An Engine and Shock Tube Study in Combustion Soot Measurement

by

Guanyu Wang

A thesis submitted in partial fulfillment
of the requirements for the degree of
Master of Science in Engineering
(Mechanical Engineering)
in the University of Michigan-Dearborn
2016

Master's Thesis Committee:

Professor Patrick Lynch, Chair
Professor Eric Ratts
Professor Oleg Zikanov

Acknowledgments

The mini-engine project is primarily supported by UM-Dearborn Institute for Advanced Vehicle Systems Seed Funding and partially supported by the American Chemical Society Petroleum Research Fund. We are grateful to M. Ahmed (LBNL) for making the Molecular Beam TOF-PIMS endstation ready for us. We are also grateful to K. Wilson (LBNL) for making the aerosol machine ready for us. Additional thanks are given to O. Kostko, T. Troy, B. Rude and N. Richards-Henderson (LBNL) for technical assistance at the Chemical Dynamics Beamline (9.0.2). The Advanced Light Source is supported by the Director, Office of Science, Office of Basic Energy Sciences, of the U.S. Department of Energy under Contract No. DE-AC02-05CH11231.

The shock tube project is supported by the American Chemical Society Petroleum Research Fund. We thank W. Fan (UM-Dearborn) for technical assistance in setting up part of the experiment system. We appreciate the inspirations from R.S. Tranter (ANL) to improve the durability of the shock tube armature.

Special thanks is given to my thesis advisor Professor Patrick Lynch. I'm grateful to his guidance in confirming the topic of my research projects, helpful advice when I encountered problems and providing me with opportunities to access valuable research resources.

Table of Contents

List of Tables

List of Figures

Abstract

Soot phenomena in combustion have been an interesting topic in combustion research for a long time. Study of soot includes identifying reaction pathways leading to soot and developing innovative techniques and apparatus to measure soot. In this research, two separate experiments are conducted to explore possible new ways to study soot formation mechanisms in combustion. The first experiment employs a miniature engine to prove the feasibility of coupling high pressure reactors with synchrotron sourced photoionization mass spectrometry and probing species concentration in the combustion chamber and the exhaust. The second experiment demonstrates the feasibility of measuring extremely low level scattering signals by employing a high repetition rate shock tube and sensitive optical components to quantitatively measure the number density and size distribution of soot generated in the shock tube. Technical challenges and solutions of conducting the two experiments will be presented in details. Results of the two experiments will be discussed and potential improvements in the future will be given regarding the results of the currents experiments.

Chapter 1. Background

1.1 Introduction

Soot can be produced from many chemical reactions concerning hydrocarbon reactants. In some research[1, 2] and industrial applications[3, 4], sooty nanoparticles are the interesting products the structure and size of which requires precise control. However, in engineering combustion applications, soot particles are usually the byproducts of combustion. Combustion generated soot is defined as carbonaceous particulates formed from gas-phase reaction process.[5] Soot particles mainly consist carbon and a small fraction of hydrogen. Generally, soot indicates inefficient combustion.[6] Had these particles completed oxidized, they would have released more energy with products CO_2 and H_2O. Meanwhile, ultrafine soot particles can penetrate into human organs and leads to some diseases like allergy and cancer.[7] The characteristics of soot that are concerned with health and environmental issues are the soot particle size, number density, morphology, chemical composition etc.[8], thus regulations of soot emissions from combustions engines mainly focus on these areas. The first US regulation on Particle Matters (PM) emitted from compression ignition (CI) engines came out in 1987 as $0.6\ g/bhp \cdot hr$, then the soot emission cap dropped gradually to $0.01\ g/bhp \cdot hr$ in 2007 and this standard has been kept to today.[9] The soot emission regulations stand for the technical improvements in soot control and mitigation in engine combustion and drive the development of more advanced techniques to reduce soot formed from combustion. The motivation of the research project is to use experimental methods to study soot formation mechanism in intermediate phase and particle matter phase and to provide experimental

data and technical inspirations in future research of soot formation mechanism and methods to reduce soot in combustion.

1.2 Soot Formation Mechanisms

Soot formation is a complex chemical process but is also strongly affected by fluid mechanics and thermodynamics of the combustion field.[10] In addition to the inherent chemical characteristics of hydrocarbon reactants, the flow pattern of flammable mixture, the diffusion between fuel and oxidizer, which are governed by the fluid mechanics and thermodynamics, can also affect some important instant local parameters like local fuel oxidizer ratio, temperature and pressure, thus finally affects the number density, size and microstructure of the soot generated from combustion.[11–13] In the engineering area soot can be mitigated through optimized control strategies on the combustion process[14, 15] and after-treatment technologies[16, 17]. This research project focuses on the chemical aspect of the soot formation, the formation mechanism and immediate product measurement. Study in the chemical aspect of soot formation can help and guide engineering development of cleaner combustion engines and contribute to the fundamental chemical science.

While soot has been studied for several decades, part of its formation mechanism still remains unclear. It is commonly believed that there are four steps for hydrocarbon fuels to form soot:

1. Formation of single aromatic rings.[18] In the reaction system where no simple aromatic functional groups (like benzene, naphthalene etc.) exist in the reactants, single aromatic rings are often generated from decomposition and recombination of hydrocarbons. An example of this is the aromatic formation mechanism of self-combination of propargyl in methane flame[5, 6]. The generated single aromatic rings will then come to the second step of soot formation where single rings grow to polyaromatic hydrocarbons (PAH). For reaction system which

contains aromatic fuels, the availability of aromatic rings is sufficient so the formation of soot precursors is usually much easier than non-aromatic fuels.

2. Growth from single aromatic rings to PAHs, which are often identified as soot precursors[18]. One of the most famous formation mechanism of soot precursors is the hydrogen-abstraction-acetylene-addition (HACA) mechanism.[4, 5] The HACA mechanism reveals in the growing process of single aromatic rings phenyl acetylenes formed through collision of phenyl radicals and acetylene molecules will further add another acetylene molecule either on the C4 chain[22] or a second acetylene addition to the radical center shifted C_8H_7 intermediate[23] through hydrogen immigration[24]. The C_{10} aromatic intermediate then goes through cyclization reaction to form naphthalene. It should be noted that the original HACA route proposed by Frenklach[7, 11] has been ruled out by Ahmed et al. through mass spectrometry experiments[26]. In the growing process from small aromatic molecules to large cyclic compounds, the C/H ratio of a single molecules drops with increase of the molecular weight and finally form carbonaceous soot precursors.

3. Nucleation and coagulation of soot precursors. These precursors whose molecular weight is in the range of 500-1000 amu, gain weight to particle level by absorbing gas phase species in the nucleation process. Coagulation also happens among small particles during which number of particles decrease while sizes of remaining particles increase significantly.

4. Dehydrogenation and oxidation of newly formed particles. [18]

1.3 Background and Motivation of the Research

In this research, studies are focused on two aspects of the soot formation process, the very early intermediate species phase and the particle matter phase. In the early intermediate species phase,

research efforts can be put into revealing kinetic pathways and developing kinetic models[13–15], or making predictive calculations based kinetics models[16–18] etc. One of the interesting aspects is identifying species and measuring species concentration[19–21], which are important steps towards developing accurate kinetic models. Usually the identification and measurement is one of the most difficult steps in combustion experiments, because there are typically thousands of elementary reactions happening in a short period of time while thousands of intermediate species and radicals are produced and consumed with all these reactions, especially for some radicals which have extremely low concentrations, yet still provide some important pathways. In the particle matter phase, some interesting topics are studying micro structures of soot particles[36], [37], engineering developments and evaluation of particle filters[38], [39] and particle size and concentration within the soot field[40], [41].

In general, measurement methods within all soot formation phases can be classified into ex-situ methods and in-situ methods. Ex-situ measurements typically take samples from the soot field and study the properties of the sample elsewhere. An examples of ex-situ methods is mass spectrometry[35], [42]–[50], which is used to measure concentrations of species including soot related intermediate species and soot particles. Ex-situ techniques also include some advanced magnification techniques, like Transmission Electron Microscopy (TEM)[26, 27] and Atomic Force Microscopy (AFM)[27, 28] to study microcosmic morphologies of soot particles. In-situ techniques directly measure the properties of the soot field with little or no disturbance. Laser diagnostics are some useful in-situ techniques, which has many branches like laser-induced fluorescence (LIF) and laser-induced incandescence (LII)[54]–[56], Laser extinction[31, 32] and laser scattering[57] methods to measure the in-situ, spatial-resolved soot volume fraction.

For the task of making measurements in the intermediate species phase, mass spectrometry has

high sensitivity and time resolution, and is not limited to specific species, thus is an ideal technique in developing accurate kinetic models. To use mass spectrometry techniques, ionization of molecules is always the first step. Electron ionization (EI) is a more common way in ionizing molecules, yet the disadvantage of this method are fragmentation interference and difficulties in identifying molecules with same mass charge ratio due to low resolution in the ionization energy.[36–38] In comparison, photoionization (PI) mass spectrometry is less used than EI due to reasons like higher complexity, usually much lower signal level and higher cost, but on the other hand PI has almost no fragmentation problems and higher resolution in ionization energy, so that isomers and/or molecules with same mass charge ratio can be distinguished by photoionization efficiency (PIE) curves.[39, 40] Synchrotron sourced PIMS not only has the advantages of PIMS, but is also more superior in the tunability and intensity of the ionization light. However due to its complexity, currently synchrotron sourced PIMS has been employed mostly by researchers with low pressure reactors like flames[15, 17, 41], flow reactors[46], tubular nozzles[47] and jet stirred reactors[20, 21], while high pressure reactors are much less coupled with synchrotron sourced PIMS. Some published experiments using high pressure with synchrotron sourced PIMS include coupling shock tubes[35] and high pressure flow reactors[50] etc. One of the reasons for conducting combustion experiments at high pressure is because combustion applications in industry are usually at high pressures. For example, peak pressure in diesel engines are over hundreds of bars, gas turbines always run at over 100 bars. Meanwhile the high pressure combustion is also interesting to researchers in the aspect that at high pressures, the reaction rate of many elementary pathways changes dramatically with pressure, so the same reactants could have totally different reaction mechanisms between high and low pressures, thus it is very beneficial to study combustion directly in the high pressure range.

With the motivation of expanding the usage of PIMS to measure soot-related intermediate species in high pressure combustion, we conduct a pilot study in coupling another high pressure reactor, an IC engine, with synchrotron sourced PIMS at the Advanced Light Source (ALS) of the Lawrence Berkley National Laboratory (LBNL). The aim of the experiment is to measure species concentration in the engine combustion chamber and the exhaust gas, both on the molecular beam machine developed by M. Ahmed (LBNL) (See Ref [64] for more details) and the aerosol machine developed by K. Wilson (LBNL) [65], and to inspire more experiments in employing synchrotron sourced PIMS in high pressure combustion.

Laser scattering technique is one of the powerful methods to measure soot particle size on-site in the particle matter phase. Scattering signal is difficult to measure because the scattered light is so weak that the signal to noise level is often very low. Optical filters and proper photo sensors (often photomultiplier tubes) are required to successfully measure scattered light. A laser scattering study of soot formed in flame is conducted by Yang et al in 2005[57]. In the laser scattering experiment related to this research, soot is formed in a shock tube which is much leaner than the concentrations of Yang's experiment, thus potentially has much lower signal to noise ratio. To solve the problem of low signal to noise ratio, a possible way is to try summing up results from hundreds of experiments at the same condition. The assembling cancels random noises and adds up real scattering signals. However, shock tube experiments are usually very time-consuming and the repeatability of conditions is hard to control due to the variations of burst style of the diaphragm and thus the idea of summing up results is hard to realize. Here in this research, employment of a high repetition rate shock tube could partially solve the two problems of the diaphragm style shock tubes mentioned above, and details of high repetition shock tube will be introduced in Section 2.

Objectives of the research are:

a) Measuring species and concentrations in the engine generated high pressure combustion in both the intermediate species phase and the particle matter phase using synchrotron sourced PIMS.

b) Measuring size of soot particles generated in shock tube using laser scattering techniques.

Chapter 2 focuses on the experimental setup of the engine and shock experiments. Chapter 3 presents and discusses the results from the two experiments. Chapter 4 summarizes the research project, makes conclusions and suggests future works in the proceeding studies.

Chapter 2. Experimental

2.1 Miniature Engine Project

2.1.1 Experiment Preparation and Setup

The design of the experiment is conceptually broken down into the configuration of the reactor, the development of the sampling techniques, the analysis techniques and some other engineering efforts. The reactor chosen for the experiment is a miniature model airplane IC engine. Samples are taken through an orifice on the cylinder head and the exhaust port. The analyzer used is the synchrotron sourced PIMS apparatus at the Lawrence Berkeley National Laboratory. Engineering effort has been taken in damping noises, venting exhaust gases and monitoring hazardous gases. All the experimental preparations and setup will be introduced in detail in the following sections.

2.1.1.1 Engine Configuration

The reactor of the experiment is a commercial two-stroke miniature IC engine (O.S. Engine 46AX II) with a customized cylinder head. Displacement of the engine is 7.45 cc; the stroke is 19.6mm. The engine is fueled by methanol (ACS grade, VWR) with castor oil (5-20% by volume, McMaster-Carr) added as lubricant. The instant peak in-cylinder pressure is ~15 bar. The schematic of the customized cylinder head is shown in Figure 2-2. A glow plug is screwed into Port A. While the engine starts, a glow igniter is connected to the glow plug, providing sufficient energy to ignite the fuel, and is removed after the engine starts. Port B is a screw port for the pressure transducer (PCB 105C12) recording the time resolved in-cylinder pressure data. Port C is a 1/4-28 screw port for screwed orifices (Dia. 15-30μm, Lenox Laser). Teflon tapes or O-rings are

used to seal the threads, and 30μm is the largest orifice diameter that could be applied to this apparatus to sample gases from the combustion chamber while still sustain the running of the engine, because any larger orifice used will decrease the peak in-cylinder pressure to be lower than the ignition limit. Orifices become clogged with oil over time and were checked and replaced after each experiment.

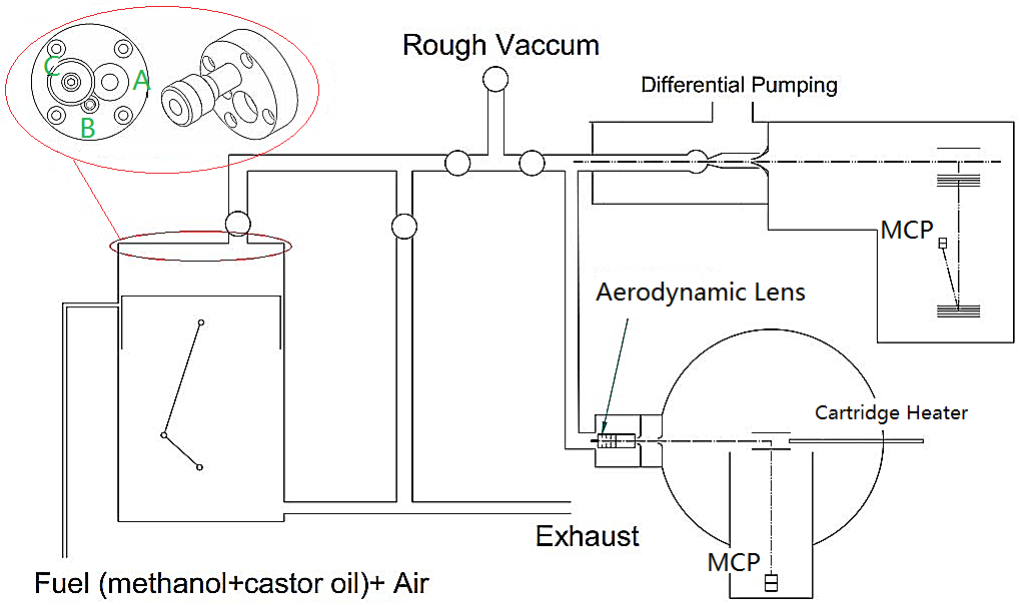

Figure 2-1 Schematic of the Engine Experiment

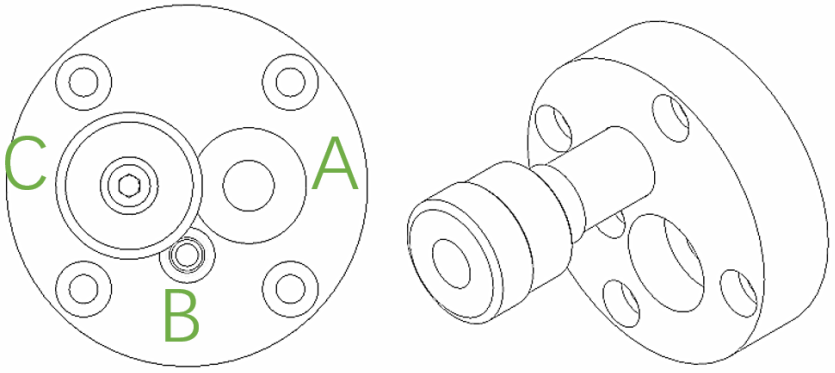

Figure 2-2 Customized Engine Cylinder Head with Sampling Port

In-cylinder gases (products and quenched intermediates) are designed to be sampled from high pressure (~15 bar) on the combustion chamber's side through the orifice to the low pressure (<300 Torr) in the sampling line connected between the sampling port and the entrance of the PIMS. Samples undergo an expansion process through the orifice, and the temperature of the sample gases drops from the hot reaction zone temperature to a cold level in the sampling line, thus some intermediate products are frozen and able to be detected by the PIMS. The use of the orifice also maintains a relatively low pressure outside the PIMS inlet, which is preferable than high pressures that could cause failures of the PIMS.

There's also a branch from the engine exhaust line to the PIMS. This line is much easier to build and is used to study sooty aerosols on the aerosol machine and to compare with the chamber samples on the molecular beam machine. More details in sampling from engine exhaust are in the following sections.

2.1.1.2 Noise Damping and Exhaust Ventilation

Some of challenges of successfully coupling the miniature engine to the PIMS at ALS are some engineering and safety considerations concerning running an engine in an indoor environment. Noises should be damped and exhausts should be properly ventilated to make the engine run safely and comfortably in a laboratory, so some preparation work was done before the experiments were conducted at ALS.

The engine is mounted onto the top of a cart to have the mobility to travel between PIMS endstations, and a noise damping box is made to absorb noises from the engine. The noise damping box is made of PVC plastic and acrylic, both of which have a satisfactory strength and stiffness in a relatively hot environment (35-40ºC) surrounding the engine while the maximum temperature on the engine's outer surface is about 150 ºC. Also, the acrylic top and front of the noise dumping

box is transparent, so researchers are able to see the engine running directly and prevent some potential accidents as early as possible, e.g., damping box melting, fuel pipe leaking. Feedthroughs and bulkheads are made on the box wall to give access to all pipelines and electronics. There's also a thin rubber padding under the engine base to dump vibrations from conducting to the cart body.

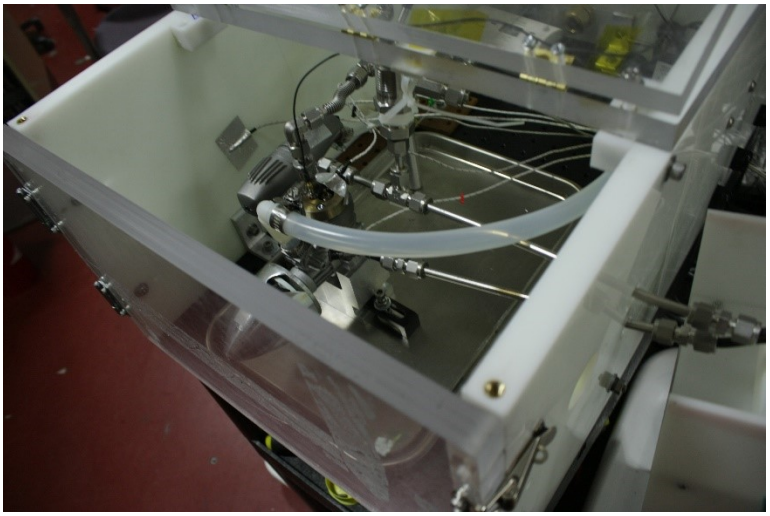

Figure 2-3 Noise Dumping Box

Properly ventilation of engine exhaust is realized by plumbing an exhaust line from the engine exhaust port to the vent lines in lab. The vent line should have enough venting capacity or the clogged exhaust gases will stop the engine. Because castor oil is used in the fuel as lubricant, there is a huge amount burnt and unburnt castor oil in the engine exhaust. To not damage the PIMS machines, an inline oil filter is mounted at the upstream side of the exhaust pipe. The oil filter lowers the castor oil concentration in the exhaust gas significantly, while on the other hand absorbs other species in the exhaust gas which are desired to be seen in the mass spectra. Usage of the filter decreases the overall signal level in the exhaust gas and this effect will be illustrated in Chapter 3. Also, a cold trap is in series with the oil filter to condense unburnt methanol and some water vapor. The cold trap is customized a double-pipe heat exchanger made from Swagelok connectors and

12.7 mm and 6.35 mm stainless steel tubing with cooling media water and a chiller as the heat sink.

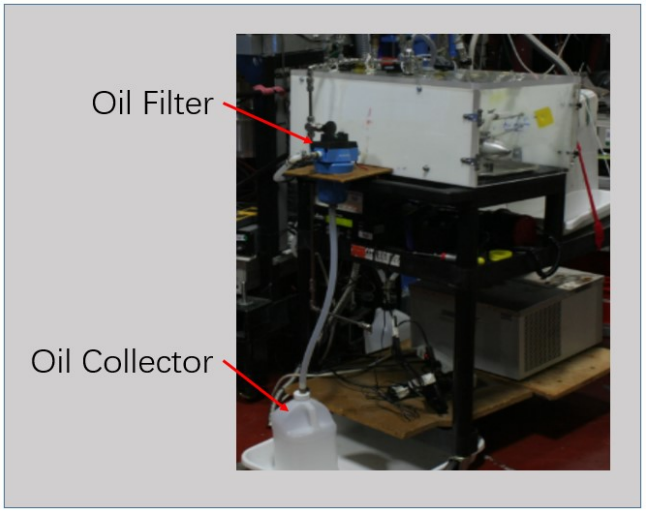

Figure 2-4 Exhaust Oil Filter

2.1.1.3 Gas Sampling Line and In-cylinder Pressure Measurement

Sampling ports of the two sampling pathways have been introduced in section 2.1.1.1 and this section introduces the sampling lines connects the sampling ports and the PIMS. The sampling port on the cylinder head is connected to the PIMS through 6.35 mm tubing and Swagelok adaptors. Other accessories on the sampling line include a pressure transducer and a pressure gauge to read pressure inside the sampling line, and a pressure relief valve to release the pressure in the line to avoid too high pressure outside the inlet of PIMS. A valve throttled oil pump is continuously pumping gas from the sampling line to keep a pretty low pressure (ideally ~100 Torr) inside the sampling line. The long length of the sampling line provides enough spaces for all the functions above, but on the other hand makes the travel time from the orifice on the cylinder head to the PIMS too long so any quenched radicals will have time to recombine thus precludes the detection of any radical species formed in the cylinder in this pilot study. This effect will be shown in the result section.

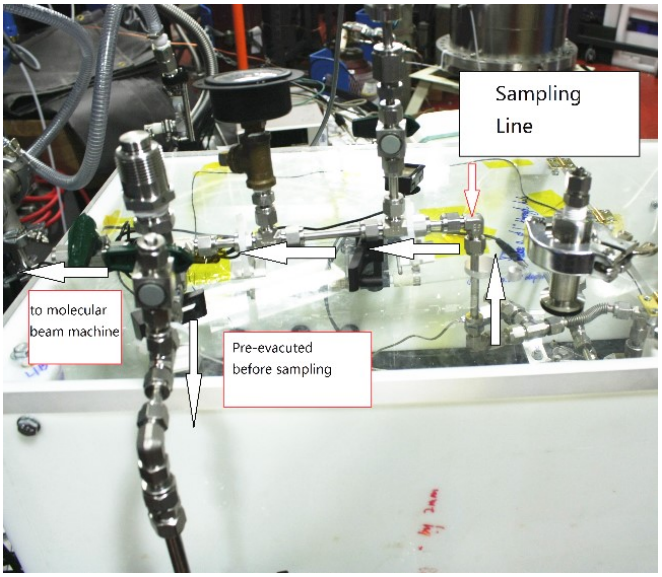

Figure 2-5 In-cylinder Gas Sampling Line

As introduced in Section 2.1.1.1 and 2.1.1.2, there's also a branch from the exhaust line to the PIMS. Details of the part from the exhaust line to the sampling line of this sampling pathway has been introduced thoroughly and rest part of the pathway is similar to the in-cylinder sampling pathway.

A high sensitivity, high time-resolution pressure transducer with a wide measurement range is required to accurately record the in-cylinder pressure. The pressure transducer used for this experiment is type PCB 105C12, which has a rise time $\leq 0.2\mu s$ and a pressure range 0-2000 psi. The pressure transducer is mounted onto port B in Figure 2-1 as introduced in Section 2.1.1.1, and its electrical signal is amplified by a pre-amplifier (PCB 482C05) before it is sent to the data acquisition card (Measurement Computing 1608-FS) which has a maximum sampling rate of 50 kHz. The adequacy of the in-cylinder pressure acquisition system is shown in the result section.

2.1.1.4 Hazardous Gas Monitoring and Safety Features

The engine should be able to stop immediately from the control desk when emergency happens. The emergency stop function is realized by a solenoid valve in the air supply line and is controlled

remotely by a button at the experimental workstation. Cutting off the air line is a faster way to stop the engine than cutting off the fuel line by practice. When the button is pressed, the engine will stop within 1s and this should save the experiment from most potential failures.

Hazardous gases should be monitored to maintain a safe operation environment. There are several hazardous gases related to engines and the most encountered one in this project is carbon monoxide. CO indicates insufficient oxygen, and is hazardous both in toxicity and flammability. For the experimental setup, if CO appears, it should first gather its concentration inside the noise damping box. So a CO monitor is placed inside the noise dumping box and once the CO concentration inside the box is higher than normal, it will send out alarms and the engine should be stopped immediately to check for problems. Usually the excessive CO is caused by worn of the engine or leakage in the exhaust line.

2.1.1.5 Molecular Beam Machine and Aerosol Machine

After all the preparation work has been finished at UM-Dearborn, the system was taken to ALS and connected to the Molecular Beam Machine and Aerosol Machine. The connection schematic is shown in 2-9. It should be noted that although on the experiment schematic the engine seems to be able to switch between the two endstations, the engine was connected to only one of the endstation at a time at different phase of the experiment.

The quenching process of hot products and intermediates from the combustion chamber side to the sampling line side has been introduced in detail in previous sections. While the pressure inside the combustion chamber is as high as ~15 bar, the pressure of the ion source of the mass spectrometer were safely maintained at $<10^{-5}$ Torr and the connection to the synchrotron VUV source at $<10^{-7}$ Torr. In separate experiments, exhaust gases were sampled into the sampling line as described previously. Exhaust gases contained large concentrations of castor oil and methanol so a coalescing

oil filter and cold trap were used to protect the molecular beams endstation and the aerosol mass spectrometer. This combined with the relatively large size of the sampling line greatly reduced signal levels, however some product species were still present with detectable concentrations.

The PIMS devices at ALS are the time-of-flight (TOF) type mass spectrometers. For illustration, in the molecular beam machine in Figure 2-6, sample gases enter the differential pumping chamber through the inlet port of the machine and only a small portion pass through the skimmer and finally enter the ionization chamber. In the ionization chamber, molecules are ionized by an incident Vacuum Ultraviolet beam. The ions are accelerated in the extracting electric field and gain approximately the same amount of kinetic energy after getting out of the electric field. Because the ions have the same kinetic energy but different mass to charge ratio, they fly at different speeds inside the chamber thus their time of flight inside the chamber before they finally hit the multi-channel plate (MCP) are different and the TOF is only a function of mass charge ratio. Thus by recording the number of charges the MCP receives at each time instant, the molecular beam machine is able to count number of molecules at each mass charge ratio to infer the species and calculate their concentration if proper calibration is available. Also, the VUV incident energy is tunable, so by sweeping from low to high ionization energies, species of the same mass charge ratio can be distinguished by their difference in the ionization threshold.

The working principles of the aerosol machine[66] is partially similar to that of the molecular beam machine but has some of its uniqueness to work well with higher weight molecules and aerosols. When particles flow into the aerosol machine through a 200 μm i.d. flow rate limiting orifice, they enter an aerodynamic lens system modeled after Liu and coworkers[67], [68]. Particles are focused into the final 3.00mm nozzle after pass through the aerodynamic lens and enters a two-stage differential pumping chamber so that the final amount of aerosol particles entering into the

ionization region is controlled to a very small amount to protect the device and avoid saturating the MCP detector. There is a cartridge heater in the ionization region that evaporates the impinging aerosol particles into vapor plume. The vapor plume is then ionized by the incident VUV and ions go through a similar process as in the molecular beam machine and the mass charge ratio of each aerosol particles are determined in the same manner.

2.1.1.6 Experiment Conditions

The experiment is implemented with two controlled parameters, the castor oil concentration in the fuel and the engine r.p.m. Each of the two parameters has 3 levels. The castor oil concentrations are lean (5%), medium (10%) and rich (17.5%), the engine r.p.m. ranges are low (3500–4500 r.p.m.), medium (4500–7000 r.p.m.) and high (7000–9700 r.p.m.). Experiments are conducted under conditions from different combinations of the 2 parameters.

Results can be compared between in-cylinder sample and exhaust sample at the same experiment condition, or among different conditions but sampled from the same location. Difference from any comparisons can be valuable to infer some chemical reaction pathways and sooty aerosol formation mechanisms in the exhaust gas, and all of these can serve to prove the effectiveness the effort to couple the engine combustion chamber to the synchrotron sourced PIMS.

Preparation of fuel is done in the chemistry lab at ALS. Fuel is composed by methanol and castor oil where the castor oil serves as lubricant and will not be burnt completely. Fraction of castor oil in the fuel affects the temperature and friction of the engine combustion chamber wall and thus affects the reactions inside the chamber. For example, by practice the leaner lubrication fuel used, the higher CO concentration is expected in the exhaust. Controlling of engine speed is done by adjusting the air fuel ratio, and this can be done by properly adjust the needle valve on the fuel supply line and the throttle on the air intake. Once the throttle and the needle valve position is

fixed, the engine r.p.m. will be fixed at a relative stable value and there's not too much adjustability. A simple rule is the low the air fuel ratio, the lower the engine r.p.m., but too high air fuel ratio will cause engine suddenly stall at very high speed. Detailed fuel preparation procedure and speed control strategies are shown in Appendix A.

2.1.1.7 One-dimensional and Two-dimensional Scans

Besides the two control parameters of the engine, photon energy of the VUV-PIMS is also an important parameter affecting the final mass spectrum. All molecules and aerosols species have their own ionization threshold and only when the photon energy of the incident VUV is higher than the ionization threshold of a species that its molecule can be ionized and contribute to the mass spectrum at a specific mass charge ratio, all otherwise the species can barely be reflected on the mass spectrum, even though it might have a very high concentration. The photon energy range of incident VUV used on the PIMS endstations is determined by the synchrotron at ALS is used from 8-15 eV and has an excellent energy resolution of 0.05 eV. The wide range and fine energy resolution in the photon energy is extremely helpful in avoiding unwanted species of huge concentration. For example, O_2 is sufficient either from the in-cylinder or exhaust gas sample, because the two stroke engine is very inefficient and has some amount of unburned air fuel mixture exhausted even though the engine is running in globally rich conditions. However, O_2 is not an interesting species in this experiment. In order to lower the risk of the Molecular Beam Machine being saturated at m/z=32 just because of abundant O_2, the photon energy is chosen under 12 eV[69] in some experiments. Another benefit of wide range and high energy resolution of the VUV photon energy is the ability in distinguishing species with the same mass charge ratio. For example, methanol (CH_3OH) and oxygen (O_2) both have molecular weight 32 but different ionization energies (IE) that $IE_{methanol}=10.85\ eV$[70] and $IE_{oxygen}=12.07\ eV$[69]. To identify the fraction of

CH_3OH and O_2 at m/z=32 on the mass spectrum, one just need to split the photoionization efficiency (PIE) curve by 10.85 eV and 12.07 eV, and the amount of molecules between 10.85 eV and 12.07 eV are methanol and higher than 12.07 eV are oxygen. The power of PIE curves will be shown in detail in the result section.

In this experiment, two types of scan are conducted: one-dimensional scan and two-dimensional scan. One-dimensional scan is acquired by setting the photon energy of the VUV at a fixed value and acquire the mass spectrum under the ionization energy. Two-dimensional scan, which is also called the PIE scan, is the stack of one-dimensional scans of the same experiment condition at increasing ionization energy with a resolution of 0.05 eV. The two-dimensional scan records how many molecules are detected at each mass charge ratio (m/z) with the increasing ionization energy, so if a slice is taken from a two-dimensional scan at a specific mass charge ratio (m/z), it is actually the PIE curve at that m/z.

2.2 Laser Scattering Experiments with High Repetition Rate Shock Tube

2.2.1 The High Repetition Rate Shock at UM-Dearborn

The laser scattering experiment is aimed at quantitatively measuring soot size distribution generated from a shock tube. Shock tubes are one of the most common apparatus in studying supersonic fluid mechanics and chemical reactions[52–54]. A schematic of the traditional type of shock tubes is shown in Figure 2-6. The traditional shock tube consists of a high pressure driver section and a low pressure driven section. The two sections are separated by a diaphragm. Once the diaphragm between the driver and driven section is broken or removed, the high pressure driver gas will come into contact to the low pressure driven gas and generates a shock wave which propagates inside the shock tube. When the shock wave hits the enwall of the driven section, the pressure and temperature near the endwall will increase to a high level typically within several to

tens of microseconds[60, 61] to initiate reactions and skip the slow process waiting for temperature to rise to the desired level which is common to other reactors. Fast rise in the temperature helps to get rid of many unwanted species and reaction pathways happening in the low temperature region and makes things easier for researchers to focus on the reactions they want. There are usually several time of arrival sensors on the driven section side wall to measure the shock wave velocity and a diagnostic window area at the end of the driven section to study the reaction field.

As introduced previously, shock tube has high-pressure capabilities and high controllability in the reaction pressure, temperature and species, thus is an ideal apparatus for studying combustion and soot formation mechanisms, while on the other hand it is time-consuming and has shot-to-shot variations, especially for the commonly used diaphragm style shock tubes. To overcome the drawbacks of diaphragm style shock tube, a diaphragmless high repetition rate shock tube (HRRST) has been built at University of Michigan-Dearborn.

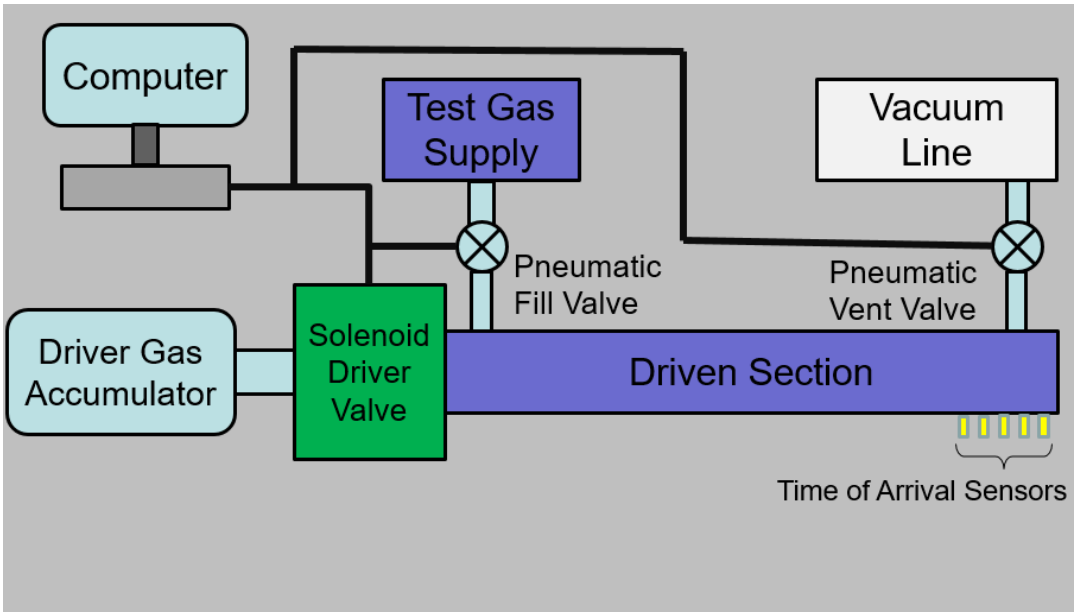

Figure 2-6 HRRST Schematic

Unlike the traditional shock tube, which is usually large and uses diaphragm to separate the driver

and driven section, the HRRST employs a customized solenoid valve to separate the driver and driven section. In this way, placing and bursting a diaphragm between the driver and driven section correspond respectively to the close and open of the solenoid valve, so operators do not have to open the shock tube to replace the burst diaphragm and clean the diaphragm fragments inside the shock tube and save most of their times. Meanwhile, high repetition rate shock tube is usually designed much smaller than most diaphragm style shock tube so time is also saved on evacuating the shock tube. On the other hand, the action of a solenoid valve is more stable and predictable compared to the burst style of a diaphragm, thus the repeatability of shots at nominally the same condition is higher of the HRRST. However, the solenoid valve only works well and reliably in mini shock tubes, as a solenoid valve large enough to be compatible with a normal size shock tube (typically 10cm in inner diameter) will be very hard in development and operation. With a smaller scale, the HRRST's often have drawbacks in its short effective measurement time (typically 700-1000 μs) and boundary layer (BL) concerns as BL's growth to the shock tube center is several times faster than a normal size shock tube. The limitation in the effective measurement time requires higher level control and synchronization techniques. The growth speed of the boundary layer is pre-calculated before designing a mini shock tube to make sure enough clearance for the reactions.

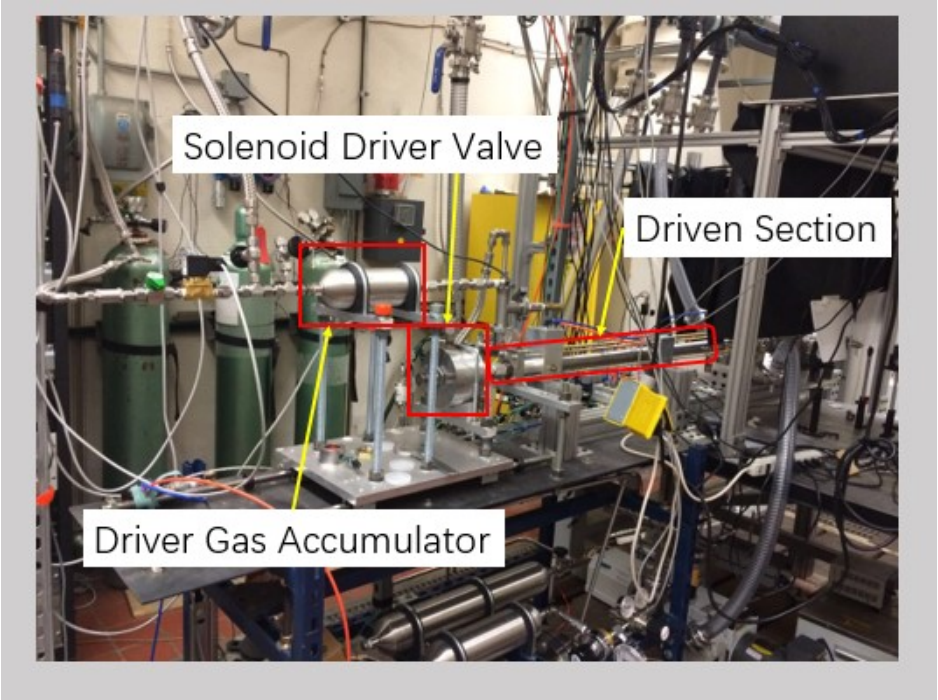

Figure 2-7 HRRST at UM-Dearborn

To take full advantage of the fast action of the solenoid valve, there are also two pneumatic valves work as the fill and vent valve of the driven section and are also able to be controlled remotely. A program written in Labview is used to control open and close of the solenoid valve and the fill and vent pneumatic valves, so that all actions including filling the driven section, firing the shock tube and evacuating the shock tube can be done automatically by following a timing diagram in the computer. Huge amount of experiment time can be saved and the probability of fault operation by personnel is also much lowered. When a specific experiment is worked on, the control program is usually coupled with the appropriate data acquisition (DAQ) and processing program, so that the DAQ and processing can be finished on the fly and give a feedback to the experimenter whether the system is working properly or not. The repetition rate of the shock tube is determined by many factors, for example, vacuum line pumping capacity, the pressure range and temperature range of interest in the shock tube, size of the shock tube and its auxiliary systems, and even data acquisition

requirements for some ultra-high frequency shock tubes, e.g., one of the HRRST at Argonne National Laboratory[76]. The ratio of pumping capacity of the vacuum line and the internal volume of the driven section has the highest effect on the total period of a single shot, because the slowest process in a firing cycle is to wait for the shock tube to be fully evacuated after a fire action. The HRRST at UM-Dearborn has a highest applicable experimental rate of 0.5 Hz (2s per shot). An example firing diagram is shown in Figure 2-10. The shock tube in Figure 2-10 runs at master mode and has a period of 3s (1/3 Hz).

Validations on the HRRST at UM-Dearborn has been taken in characterizations of the temperature and density inside the shock tube. Temperature inside the shock tube is calibrated through chemical thermometry, the dissociation of 1,1,1-fluoroethane.[77] Gas density inside this shock tube is characterized by the synchrotron sourced X-ray at the Argonne National Laboratory and is still in progress. Another HRRST developed at ANL which has an 6.35mm I.D. has already been characterized[76].

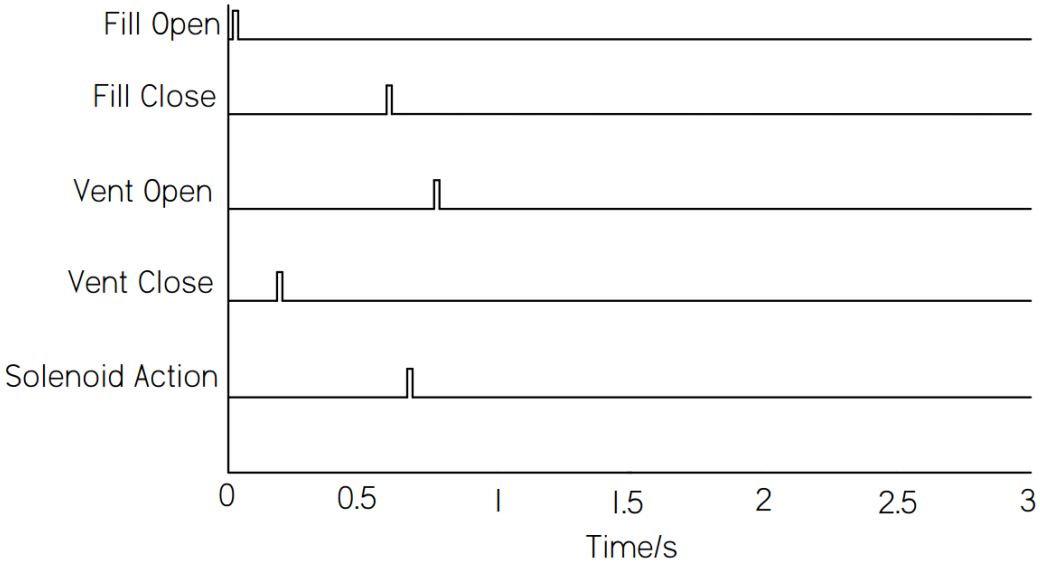

Figure 2-8 Example HRRST Valve Timing

2.2.2 Molecular Beam Sampling System

The sampling system of this experiment consists an endwall nozzle and a vacuum chamber, as shown in Figure 2-15. When shock wave arrives at the driven section endwall, high pressure builds up in that area and it pushes a small portion of gases through the endwall nozzle. The sample gas expands supersonically into the vacuum chamber and forms a molecular beam. The sample is quenched to a low enough temperature while expansion and is thus frozen at the phase when it is just pushed out of the driven section. Benefited from the feature of nozzle expansion, the sampling system is able to do time-resolved measurement of the species and concentration at the driven section endwall, which is extremely useful in inferring possible reaction pathways and calculating elementary reaction rate.

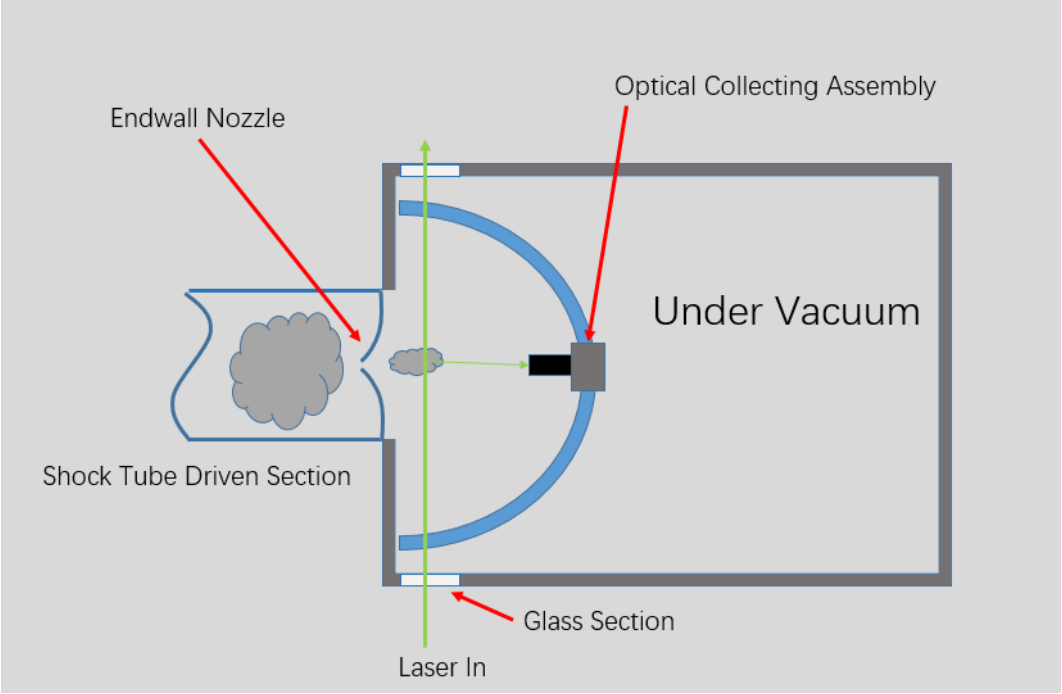

Figure 2-9 Sampling System Schematic

2.2.3 Laser Diagnostic System

The Laser Diagnostic System uses laser scattering techniques to measure the soot field. Related

theory of light scattering can be found in [78]. As shown in Figure 2-15, the laser source is a frequency-doubled Nd:YAG laser with effective wavelength λ=532 nm. The laser source does not emit continuously laser beam, but rather a double peak pulse of frequency from 1 to 5 Hz with each pulse width ~10 ns. Right after the laser source is a polarization tuner consists of a half-wave plate and a beam splitter cube. The half-wave plate tunes the polarization direction of the laser source and the beam splitter cube only transmitted the horizontally polarization component of the incident laser. In this way, the laser beam used for scattering measurement is polarized only in the horizontal direction so noise light in other polarizing directions can be filtered out by a polarizer. A portion of the total beam intensity is split and monitored by a photodiode sensor, which is used as a reference of the laser source intensity. However, this method of monitoring laser source intensity will decrease the incident laser intensity shooting into the soot cluster and lowers the scattering light signal level which is already very low. On the other hand, soot generated from the shock tube is extremely lean whose transparency can be approximated to 1 with very little error, so in the experiment the transmitted light intensity is directly used as the laser source intensity.

Scattering light from soot is collected by an optical collecting assembly shown in Figure 2-12. The polarizer in the front only allows horizontally polarized light into the optics assembly to eliminate noise light as introduced in the previous paragraph. The collecting lens is used to collect scattering signals within a small solid angle. With the experimental configuration used, the optics assembly only collects scattering light within a solid angle of ~0.124 sr, and is thus able to ensure a high enough angular resolution when fitting the scattering data at each angular position to the Mie scattering curves. The collimating lens is always used with fiber optics to ensure most of the collected light will be transmitted out of the chamber into the photomultiplier tube. Due to the extremely high sensitivity of the photomultiplier tube, cautions should be made to avoid saturating

the PMT just with reflected light. Spatial filtering techniques[79] are also used to collimate the beam and reduce diffraction.

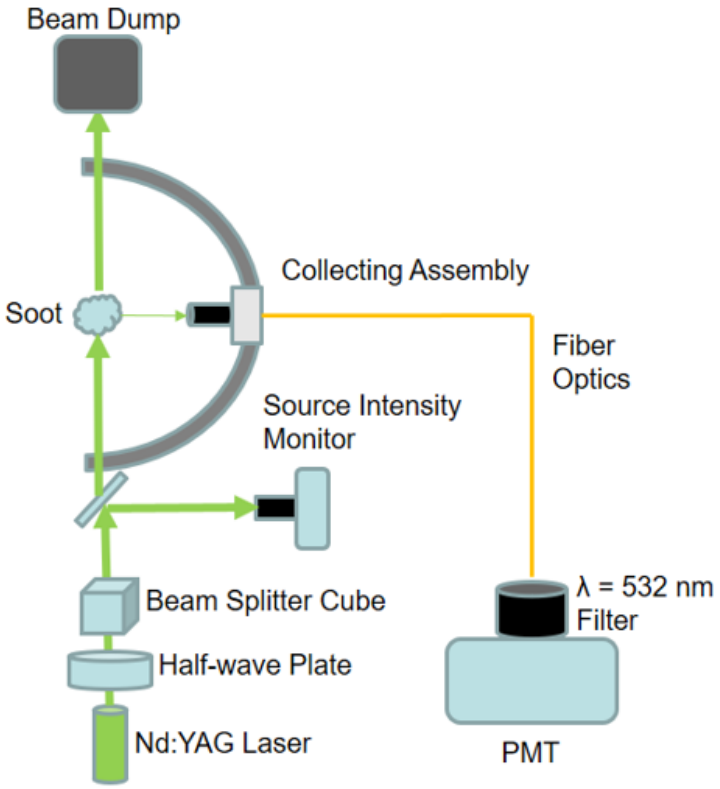

Figure 2-10 Optics Configuration

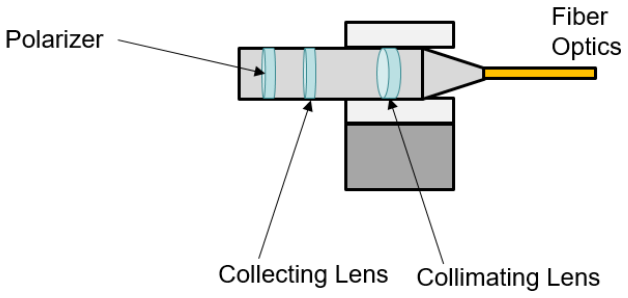

Figure 2-11 Collecting Optics Assembly

As the sampling and measurement happens inside the enclosed vacuum chamber, it is not

convenient to manually change the angle of the detector to measure scattering intensity at different angular positions like previous work done by Yang al et.[57]. To remotely repositioning the collecting optics assembly, a custom made goniometer system is made. The goniometer system consists of a stepper motor controlled by an Arduino Uno board, a semi-circular rail, a slide to transport the optical assembly, and a belt-gear transmission between the transmission and the slide. Angular range of the goniometer is from 35° to 150° due to restrictions in geometry. Angular resolution of the stepper motor is 1.8° and the goniometer takes 1972±48 (~±2.5% relative error) steps to go from 35º to 150º. This positional accuracy is acceptable and can be further improved by increasing the stiffness of the transmission and lubricating the rail. Careful calibrations of the absolute position of the optical assembly are performed before experiments.

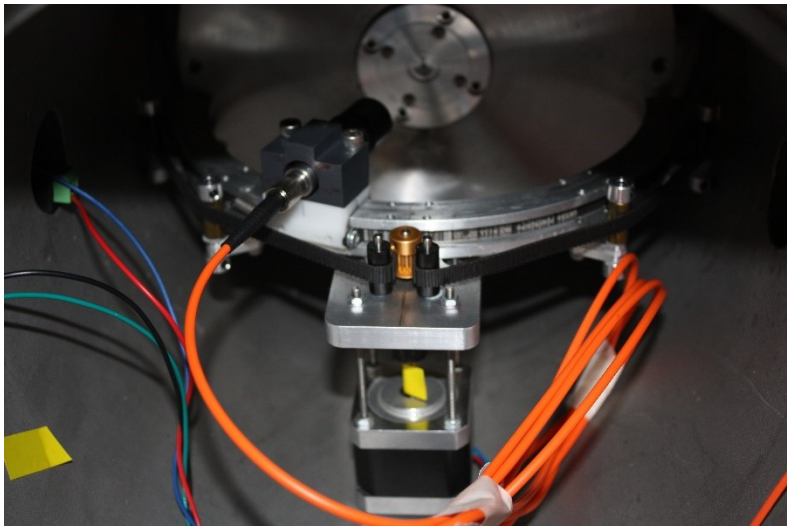

Figure 2-12 Goniometer System

2.2.4 Data Acquisition System

2.2.4.1 Data Acquisition System of the HRRST

There are both slow and fast changing data of the shock tube to be acquired. For the low speed data acquisition system, data collected are relatively steady properties, like pre-shock driver/ driven section pressure, driven section and environment temperatures etc. These data are easy to

collect and serve as a part of the reference condition of each experiment. A fast changing data that need to be collected with high sampling rate is the arrival times of the shock wave at each time-of-arrival sensor location. The time-of-arrival sensor is a special type of pressure sensor, which is not aimed at measuring pressure accurately, but instead able to record the precise time instant when there is a large disturbance in pressure. The time-of arrival sensors are mounted on to the shock tube driven section wall or the pneumatic valve body near the endwall, and are separated by a known distance. Time intervals are used to calculate the shock velocity, which is an important parameter in calculating the temperature and pressure of the reaction zone. In this experiment, the post-shock temperature is calculated by the process suggested by William C. Gardiner et al. in reference [80] Chapter 7. The steps are as follows:

1) Assume a shock front temperature T_2 and calculate the corresponding enthalpies at T_2 of all components in the driven gas. The temperature-dependent enthalpies of each species are calculated from the polynomial representation in the form:

$$\frac{H - H_0}{RT} = a + bT^{-1} + cT^{-2} + dT^{-3} + eT^{-4}$$

2) The calculated h_2 of the test gas together with the assumed T_2 can be substituted into conservation of mass, momentum and energy equations and the ideal gas law in order to calculate the shock density ratio ρ_{21}.

3) The shock wave speed can be then calculated from

$$-V_s = \sqrt{\frac{R_s(\rho_{21}T_2 - T_1)}{1 - \frac{1}{\rho_{21}}}}$$

4) The shock wave speed is compared with the shock wave speed measured by the Time-of-

Arrival sensors and corrections to new T_2 assumption is made to approach the measured shock wave speed. The converging of T_2 within 1K of accuracy is fast using this method.

5) Once the accurate T_2 is got, similar iterations steps are taken by using the conservation of mass, momentum and energy to converge the value of $u_2(1-\rho_{21})-u_5(\rho_{52}-1)$ to zero to get the accurate reflected shock temperature T_5.

6) Once the accurate post-shock temperature T_5 is got, the post shock properties like P_5 and ρ_5 can be calculated using the ideal gas law:

$$P_5 = \frac{P_1 \rho_{52} \rho_{21} T_5}{T_1}$$

$$\rho_5 = \frac{P_1 \rho_{52} \rho_{21}}{R_s T_1}$$

The calculation steps are programmed in Labview and the T_5 is calculated on the fly to give shock tube operators a quick feedback of the experimental condition.

2.2.4.2 Data Acquisition System of the Laser Scattering System

Because the laser source works at pulse mode, the timing of the shock tube should make sure when the shock wave arrives at the endwall, there should be a laser pulse shooting at the soot field and the data acquisition system should record a time range over this event. In order to do this, the shock tube should work at a slave mode and triggered by the laser. In this way, the accurate and punctual acquisition of the laser signal is important to the success of the entire experiment. As shown in Figure 2-11, the laser source intensity is monitored by a photodiode. When the laser pulse happens, the photodiode will output a voltage pulse which is recorded by the data acquisition system and also serves as the trigger to the HRRST software. The software controls the valve systems and data acquisition systems of the shock tube, so the HRRST system will start working at an appropriate

time instant without missing a laser pulse or wasting too much DAQ resources. The scattering signal is acquired by a photomultiplier tube with up to 10^7 amplification capability. Both the laser source intensity signal and the scattering signal are recorded by the National Instrument PCI-DAS4020-12 data acquisition card introduced in Section 2.1.1.1.

2.2.5 Laser Diagnostic System Validation

Due to the complexity of the experiment, validation of the functionality of the laser diagnostic system should be performed before it can be coupled with the HRRST with confidence. The validation experiment keeps everything designed for soot measurement unchanged but just replaces the soot with steam vapor from a steam jet as shown in Figure 2-15. Scattering intensities are measured at θ = 45º, 65º, 75º, 90º, 105º, 120º, 135º respectively, where θ is the angle form the downstream of the laser beam. If the scattering intensity at each angular location can be fitted to a theoretical scattering curve within a reasonable range, the function of the laser diagnostic system is validated. 5 groups of experiments are conducted at each angular location, and in each group there are 1000 acquisitions. Another 1000 acquisitions without steam have also been done at the same location to serve as a background intensity, so signals due to reflections and other environmental factors can be subtracted. Both the scattered light and the transmitted light are recorded and the ratio between the scattering light and the transmitted light $I_0 = I_{scattered}/I_{transmitted}$ is used as the representation of the scattering intensity at each location to eliminate errors caused by fluctuation in the laser source intensity. Results of the validation experiments are shown in the section 3.2.4.

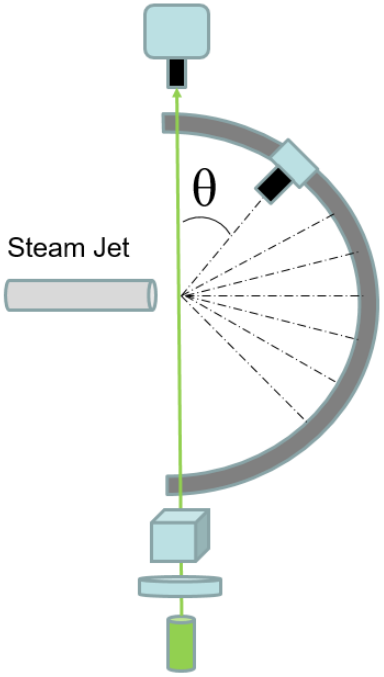

Figure 2-13 Laser Diagnostic System Validation Schematic

2.2.6 Laser Scattering Experiments with the HRRST

2.2.6.1 Experiment Setup

Figure 2-19 is the schematic of the complete experiment setup. The laser diagnostic system is coupled with the HRRST after it has been validated. The laser source pulses at nominal 1 Hz while the shock tube works at 0.25 Hz (T= 4s). At the beginning of the 4s period, the laser gun shots a pulse and is captured by the source intensity monitor photodiode. The pulse signal triggers the HRRST control system and the solenoid valve that separates the driver and driven section will open at a specified time instant so that the 3rd shot the laser gun could happen while the shock wave front is near the endwall. The data acquisition system starts to record data a little earlier than the 4th shot and covers a long enough interval to fully record the scattering process. After data recording is done, the experimental system finishes a cycle and waits for the next laser pulse to trigger the shock tube.

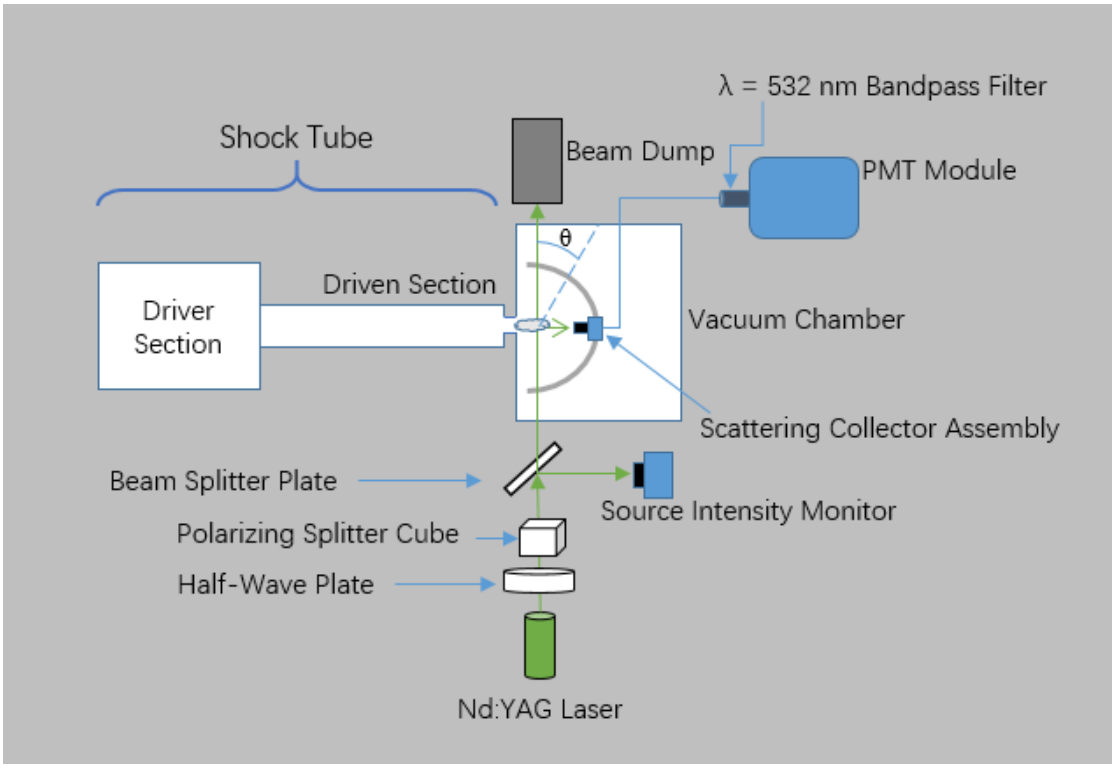

Figure 2-14 Schematic and Details of the Laser Scattering Experiment Setup

2.2.6.2 Experiment Condition

Experiments are conducted at post shock temperature T_5 = 1450K, 1560K and 1940K separately. T_5 is controlled by adjusting the driven section pressure P_1 while holding the driver section pressure P_4 near constant. 2% Acetone diluted in Argon produced from a chilled bubbler is used as the test gas. Scattering signals are mainly measured at 135° and 35° while at some temperatures scattering signal at 115° is also measured as supplement.

Chapter 3. Results and Discussion

3.1 Results and Discussion of the Miniature Engine Project

3.1.1 Validation of High Pressure Measurement Capability

Experiments were performed during an experimental campaign in December 2014. Coupling the engine apparatus with the molecular beams endstation was not trivial, and significant engineering effort was spent preparing the experiment for a synchrotron environment including sound suppression, local exhaust, minimizing flammability as described in the previous section. 18 experiments were conducted with castor oil concentration in the fuel ranging from 5% to 17.5%, and engine speed from 3500 RPM to 9700 RPM. The benefit and motivation of coupling high pressure combustion apparatus to the synchrotron sourced PIMS has been discussed in Section 1.4. During the whole miniature engine experiment, the in-cylinder pressure range is relatively stable, with a minimum pressure of ~1 bar around the bottom dead center (BDC) and a maximum pressure of ~16 bar at the top dead center (TDC). An example of the time history of the in-cylinder pressure when the engine runs at ~4700 r.p.m. is shown in Figure 3.1. Although the peak pressure ~16 bar is not as high as the pressure of industrial engines or turbines, it is already clearly distinguished from the pressure range of some low pressure reactors, e.g., flames or flow reactors, which is typically under a few bars. At the pressure of ~16 bar, some special sampling techniques (e.g., nozzle quenching) and fail-safe considerations for using synchrotron sourced PIMS with high pressure reactors are already required, so this pilot study is a good validation of the experiment design and is able to provide valuable experience for further studies.

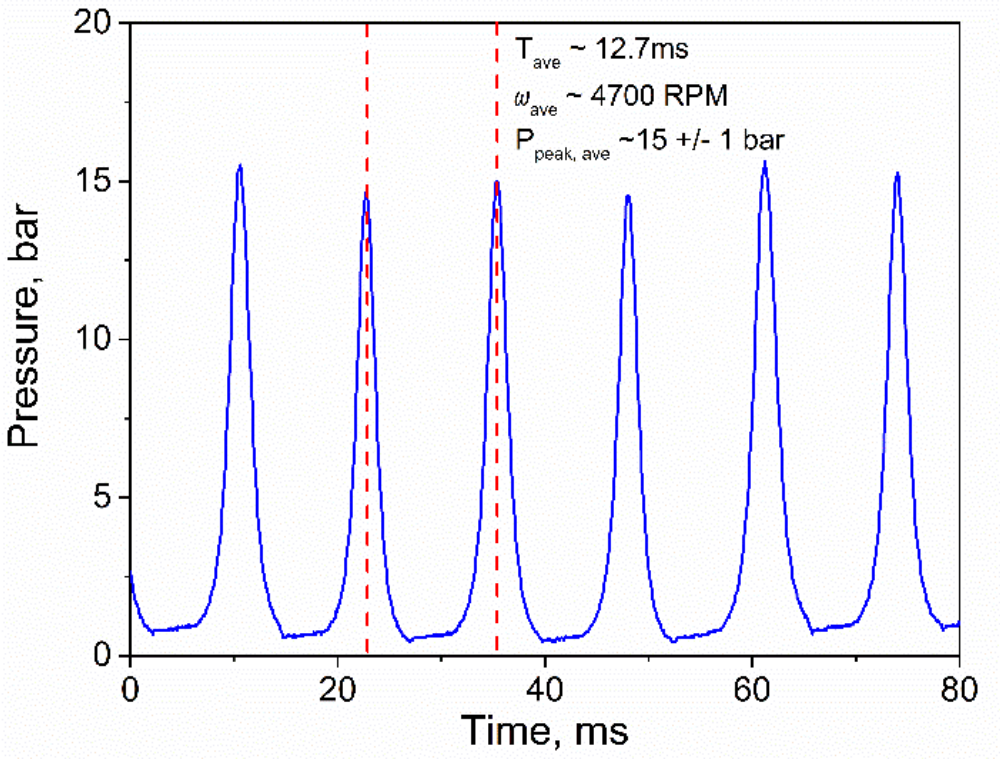

Figure 3-1 Example in-cylinder pressure profiles during engine speed 4700 RPM, fuel composition: 17.5% + 82.5% CH_3OH

3.1.2 Mass Spectra Data

Each condition was sampled through the orifice on the cylinder head as well as the exhaust. Mass spectra were acquired with ionization energy ranging from 8 eV to 13 eV, and in some experiments also at 14 eV and 15 eV. After an initial run-in period, the rotational speed was relatively constant and was monitored periodically throughout a PIE scan. It is thought that because the sampling line has a constant pressure around ~100 Torr, the largest portion of gases sampled through the orifice on the cylinder head is the reacting gas where the piston is near the top dead center (TDC). Similarly, sample gases from the exhaust line are mainly consisted of species formed in the power stroke. So differences between the in-cylinder sample and the exhaust mass spectrum are expected.

Figure 3-2 shows the mass spectrum at ionization energy 12 eV of background gases, cylinder sampled and exhaust gases at similar experimental conditions. Ion counts of Figure 3a and 3c are

the summations of 100,000 extractions and ions counts of Fig 3b is the summation of 500,000 extractions scaled by 1/5. Ionization energy 12 eV was selected as it splits the ionization energies of methanol and O_2, which would form a huge peak at m/z 32 at higher ionization energies. Figure 3-2a is the mass spectrum of background scan of helium gas at IE of 12 eV. There is almost nothing (no more than 10 counts/100,000 extractions) found on the mass spectrum as expected. Figure 3-2b shows the mass spectrum of the cylinder sampled reacting gases. The dominant species are acetone (C_3H_6O) and C_2H_3O, a fragment of acetone, almost certainly from a previous leak detection. Besides methanol (CH_3OH) and methoxy (CH_3O), a fragment of methanol, ethylene (C_2H_4), ethane (C_2H_6), and ethanol (C_2H_5OH) present. Figure 3c shows the mass spectrum of the exhaust gases. The exhaust mass spectrum contains the above species in different concentrations, but are also dominated by clusters of methanol and water[82], which obviously present from the high concentration of methanol in the exhaust of this system. Also present is acetylene (C_2H_2), formaldehyde (CH_2O), and m/z 61 which have not been definitely assigned but is possibly a methanol cluster dissociation product since the PIE curves resemble those of methanol clusters[82]. As described in Section 2.1.1.3, there's no radical found on the mass spectrum except for methoxy (CH_3O), because the sampling line is too long and most radicals recombine in their trip to the molecular beam machine. Methoxy radicals are still detectable because there is rich methanol in the reaction system which is a major source for methoxy radicals, so even after the vast majority of methoxy radicals are consumed in the sampling line, there are still a number of them entering into the molecular beam machine. Considering the effect of the long sampling line, the mass spectrum acquired in this experiment is actually a time-averaged mass spectrum. A potential improvement will be proposed in Section 4 to make the experiment system to be able to measure time-resolved species concentration from the engine chamber, so that accurate reaction

mechanisms can be inferred from the time-resolved species concentration and accurate chemical kinetic models can be developed.

Some aerosol mass spectra data are also acquired from the aerosol machine at ALS. However, because the exhaust gas sample coming into the aerosol machine still consists a considerable amount of castor oil even though the majority of it is removed from the sample by the coalescing filter, these castor oil species saturated the aerosol machine and made the identification of other aerosol species nearly impossible. Figure 3-3 shows a comparison between nebulized castor oil and exhaust gas sample got from the condition 5% castor oil in the fuel mixture and engine running at 3900 RPM.

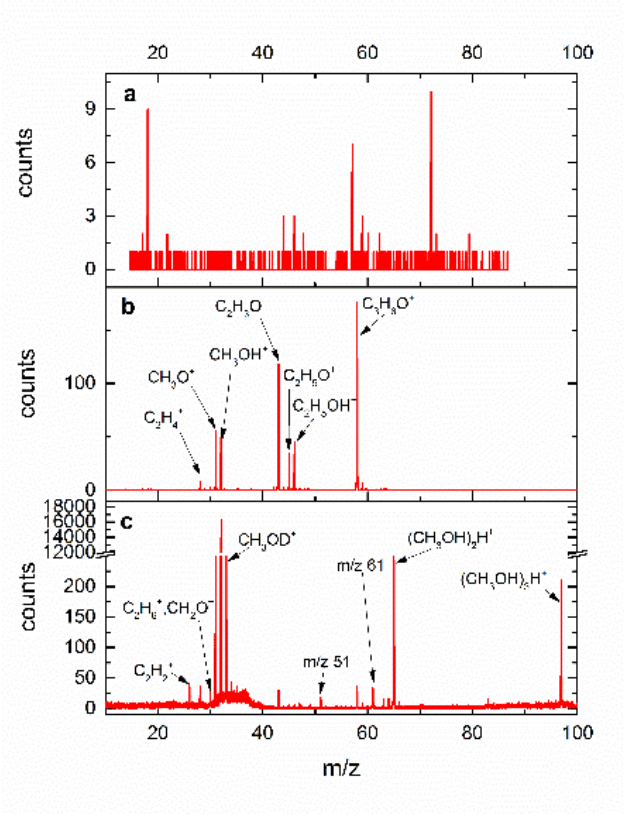

Figure 3-2 Mass spectra at ionization energy 12 eV of a) Helium with a backing pressure of 100 Torr. b) Reacting gases sampled through the orifice on the cylinder head at 4700 RPM with fuel of 17.5% castor oil and 82.5% methanol c) Exhaust gases at 4500 RPM with fuel of 17.5% castor oil and 82.5% methanol.

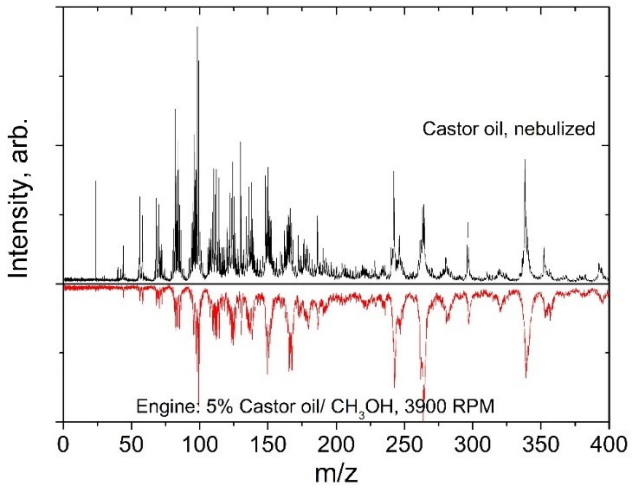

Figure 3-3 Mass Spectra of Nebulized Castor Oil and Engine Exhaust Sample

3.1.3 Photo Ionization Efficiency Curves

Figure 3-4 is a typical PIE curve, in this case m/z 30 with the engine operated at 4600±100 RPM with fuel composition of 17.5% castor oil and 82.5% methanol. Possible species of molecular weight 30 in the IC engine-based combustion system are ethane (IE = 11.52 eV[83]), formaldehyde (IE = 10.86 eV[84]), and nitric oxide (NO, IE = 9.3 eV[85]). Absolute intensity calibrations were not obtained during this campaign, so only relative and not absolute concentrations can be ascertained. Figure 3-3 shows for both in-cylinder and exhaust sampling, the PIE curves start to have some destabilizations at ~9.5 eV. However, this fluctuation is so small that it cannot indicate the appearance of NO with confidence. Then at ~10.8 eV both PIE curve start to take a significant step, which corresponds well with the ionization energy of formaldehyde, so this should be a proof of existence of formaldehyde both in the in-cylinder sample and the exhaust sample. The relative concentration of formaldehyde can be calculated as well. Finally, there is a large rise of the PIE curve just a little below 11.6 eV, which demonstrates the substantial portion of ethane at m/z 30. The drop in intensity just below 12eV is from the decrease in VUV light intensity after absorption in the beamline gas filter. The PIE curves are scaled so that the portions attributable to ethane

overlap. There is a difference between the cylinder sampled gases and the exhaust gases beyond merely signal levels, although it is clear that the signal levels in the cylinder sampled gases are extremely low.

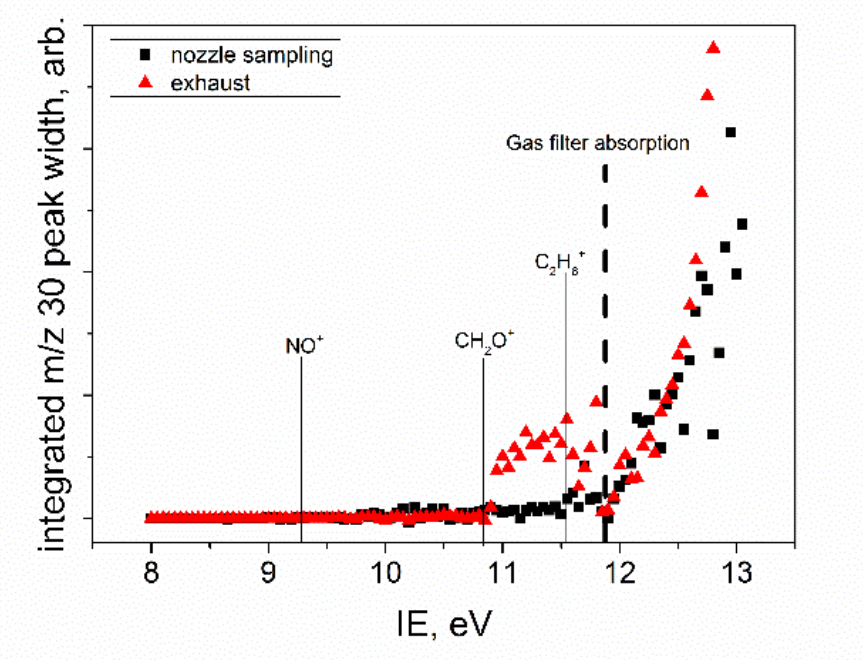

Figure 3-4 PIE curve for m/z=30 of cylinder head and exhaust sampling. Engine operated at 4600±100 r.p.m., fueled with 17.5% methanol+ 82.5% methanol.

Figure 3-5 is the PIE curves of some interesting mass peaks in Figure 3-2 c. The PIE curve of m/z 51 starts to wiggle at around 9.7 eV, but the first significant rise happens at around 10.4 eV. Thus the m/z 51 peak most likely refers to the protonated methanol water clusters with the formula $(CH_3OH)(H_2O)H+$. This is a reasonable assumption because the IC engine used is a two-stroke engine thus very inefficient, so it is possible to see unburned methanol molecules and molecule clusters in the exhaust. This assumption is also supported by the succeeding peaks at m/z 65, 83, 97, 115, 129 and 147, which are assumed to be $(CH_3OH)_2H+$, $(CH_3OH)_2(H_2O)H+$, $(CH_3OH)_3H+$, $(CH_3OH)_3(H_2O)H+$, $(CH_3OH)_3H+$, $(CH_3OH)_3(H_2O)H+$, $(CH_3OH)_4H+$ and $(CH_3OH)_4(H_2O)H+$ respectively. These assumptions are checked by their PIE curves, and the appearance energies

match the previous measurements made by Kostko and co-workers in 2008[82].

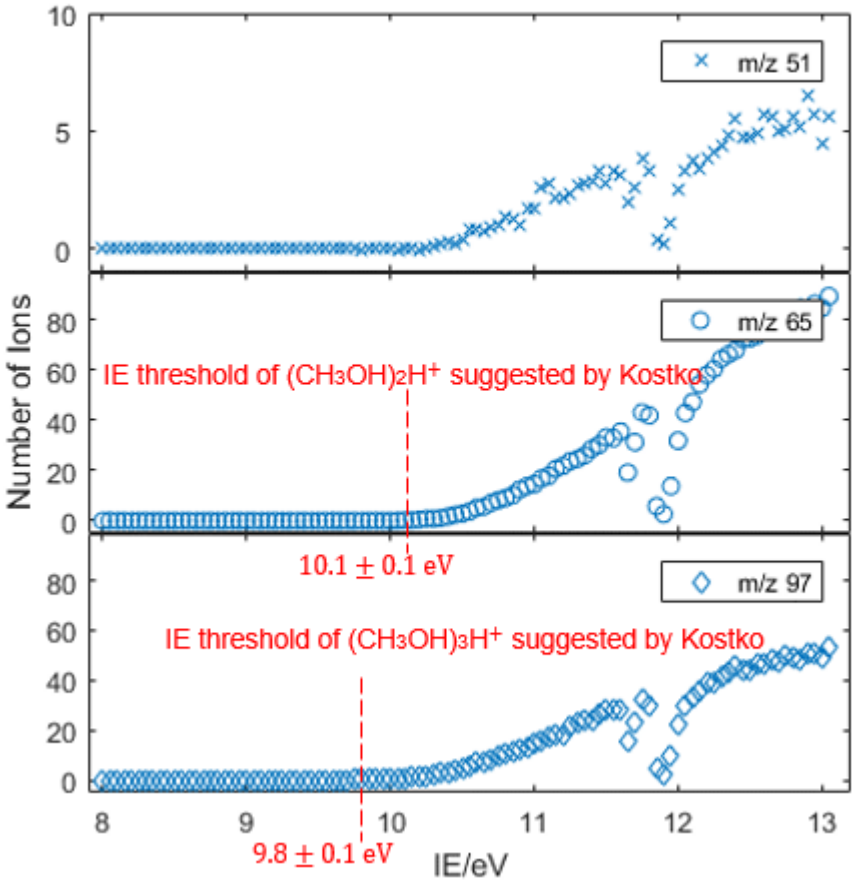

Figure 3-5 PIE curve for m/z=51, 65 and 97 of exhaust sampling. Engine operated at 4700±100 r.p.m., fueled with 17.5% methanol+ 82.5% methanol

3.1.4 Signal to Noise Level

To take advantage of the high concentration sensitivity of the synchrotron sourced PIMS, the signal-to-noise level of the mass spectra is an important specification of the designed experiments. High signal-to-noise level is helpful to acquire time-resolved species concentrations with ideal accuracy, especially of the radicals, to develop appropriate models for simulation, which is important for follow-on development in modeling and simulation.

There are two types of noise in the mass spectra, the systematic noise and the random noise. The intensity of the systematic error is generally based on the counting rate, and is thus controlled by

factors including molecular beam concentration, incident light intensity, the tuning/sensitivity of the mass spectrometer/detector, etc.[35] Factors causing systematic noises should be carefully examined and excluded before taking scans of species. On the other hand, random noises are easier to handle with the experiment design as they will cancel out over enough amount of scans on species. The engine speed was several thousand RPM during experiments and repeatability among strokes is ideal due to the characteristics of an IC engine and can also be illustrated by the pressure-time profile shown in Figure 3-1 that the variation in the in-cylinder pressure peak is only ±6.7%. Thus it only took several minutes to get enough amount of data of statistical satisfactory.

Except for lowering the noise level, another way to increase the signal to noise level is to increase the signal level. The small volume of the combustion chamber of the engine used in this experiment makes it impossible to take a large enough sample from the reacting gas while still maintains the engine running. Thus, increasing the engine size is helpful to elevate the S/N level by the taking larger samples from the combustion chamber without stopping the engine, but the engine size should still be confined within the range to operate easily in a synchrotron based environment.

Another more effective but also more challenging way to increase the signal level is to couple the sampling point directly to the mass spectrometer. Lynch et al.[35] had successfully coupled a miniature shock tube with the molecular beam mass spectrometer at the ALS in year 2013. In their design, the miniature shock tube was installed inside the differential chamber of the mass spectrometer and the skimmer of the mass spectrometer protruded ~0.75mm into the shock driven section. This sort of design will not only increase the signal level significantly, but also minimize any possible intermediate process from the reacting system to the measurement location, thus makes possible the time-resolved measurement and allows more chances to see radicals.

3.2 Results and Discussion of the High Repetition Rate Shock Tube Experiments

3.2.1 Shock Wave Speed and Endwall Pressure

The speed of shock wave in each single experiment is measured by the 6 Time-of-Arrival sensors mounted near the shock tube endwall. The Time-of Arrival sensors are spaced by 75mm and the shock wave speed can be calculated by the averaging the speed of the shock wave within each sensor spacing. Table 3.1 is an example of time intervals of a shock tube experiment at P_4= 104.4 psi, P_1= 320.4 Torr and T_1= 28.5°C, where P_4 is the driver section pressure, P_1 is the driven section pre-shock pressure and T_1 is the driven section pre-shock temperature. The average shock wave of this experiment is 792.3 m/s. The post shock temperature T_5 can be calculated using the measured shock wave speed and the algorithm mentioned in Section 2.2.

Table 3-1 Example Shock Wave Arrival Time at Different Sensor Locations

Transducer Spacing/ mm	75	75	75	75	75
Time Intervals/ μs	97.47	104.58	82.92	94.63	96.41
Shock Wave Speed ms^{-1}	769.5	717.2	904.5	792.6	777.9

Figure 3-6 is the summary of post shock conditions of a surf of shock tube experiments at $P_4 = 113 \pm 1$ psi, $P_1 = 262.8 \pm 8.5$ Torr and $T_1 = 30.2 \pm 0.35$ ℃. 253 shocks are fired and the results of 249 experiments are displayed in Figure 3.5, while 4 outliers are discarded. The post shock pressure P_5 is in the range 11.45 ± 0.48 atm (2σ accuracy), which is typical for high pressure combustion studies and the post shock temperature T_5 is in the range 1477 ± 25 K (2σ accuracy). The variation in P_5 and T_5 is sufficiently small compared with full-scale diaphragmless shock tube[86] and the HRRST at ANL[87].

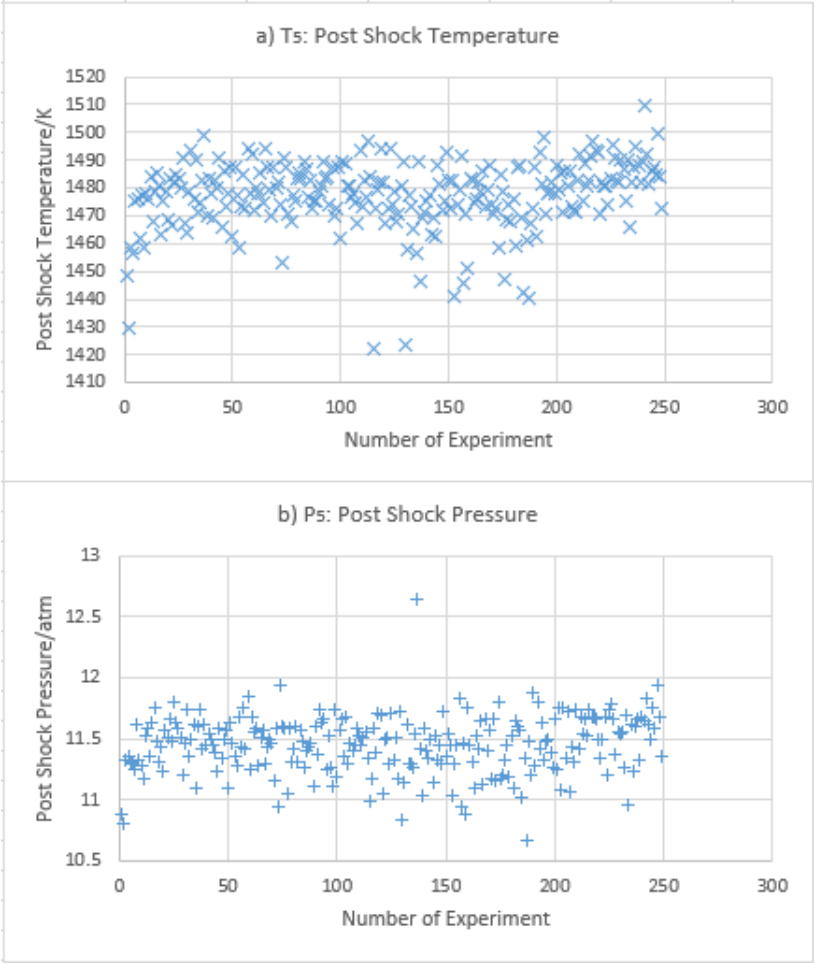

Figure 3-6 Example Post Shock Temperature and Pressure in One Surf

3.2.4 Laser Diagnostic System Validation Results

Figure 3-7 shows the scattering data measurements at 45º. Figure 3-7a is a single measurement of the transmitted light while the steam jet is turned off. There are two peaks at t=164 μs and t=201 μs and both of them are real, but also some EM noise from the laser flash lamp earlier. Figure 3-7b is a single background scan at the same time window with Figure 3-7a, while the steam jet is also turned off (i.e., the summation of any possible reflections and environmental affects). Similarly, Figure 3-7d and 3-7e are single measurements of transmitted light and scattered light respectively with the steam jet turned on. If any reflection or scattering signals are detected, they should be found at the same time instant when the peaks in the transmitted light appears. However,

both Figure 3-7b and 3-7d show poor signal to noise levels and it is impossible to state the observation of any reflected or scattering signal with confidence. This problem could be solved if results of hundreds of experiments at the same condition are summed up (i.e., summing up the results in Figure 3-7b and 3-7e). The summation cancels out random noises while keeps the real signal, thus enhancing the S/N value significantly by simultaneously increasing the numerator and decreasing the denominator.

The enhancement is well illustrated by Figure 3-7c and Figure 3-7f, which are the summed up intensity over 1000 experiments at the same condition of the background reflection intensity and the scattering intensity respectively. The S/N level of the scattering signal over 1000 experiments is high enough while the S/N level of the reflected signal is still very low even after 1000 times summations. The wider peak in the summed up scattering signal than the transmitted signal is due to a ~15 μs decay time of the PMT. Two conclusions can be drawn from the comparison. 1) The measurement of the scattering signal from extremely lean particles is feasible by summing up over many experiments. 2) The efforts to reduce reflections are effective and the PMT is free from the potential signal distortion by saturation from just background reflections. Another point that needs to be noted is the benefit of summing up hundreds of signals to promote the S/N level is only cost-effective by taking advantages of high repetition rate shock tubes. For example, with the HRRST, 1000 experiments can be done in ~50 minutes at 0.33 Hz (the typical running conditions of the UM-Dearborn HRRST).

Another thing needs to be mentioned is the double-peak phenomenon in the laser beam per shot. As mentioned earlier, both peaks are real and the time intervals between the two peaks varies slightly shot-to-shot. When assembling single experiments, single shots are aligned by the time instant of the second peak and thus causes slight misalignment in the first peak and makes the first

scattering peak a little wider than the second peak, as shown in Figure 3-7f. Meanwhile, either of the two peaks in the transmitted light can be larger than the other one, but not always be like in Figure 3-7a and 3-7d, where the first peak is much greater than the second peak. In fact, photon energy is approximately evenly distributed between the two peaks, which is proved by the similar intensity of the 1st and 2nd scattering peaks in Figure 3-7f.

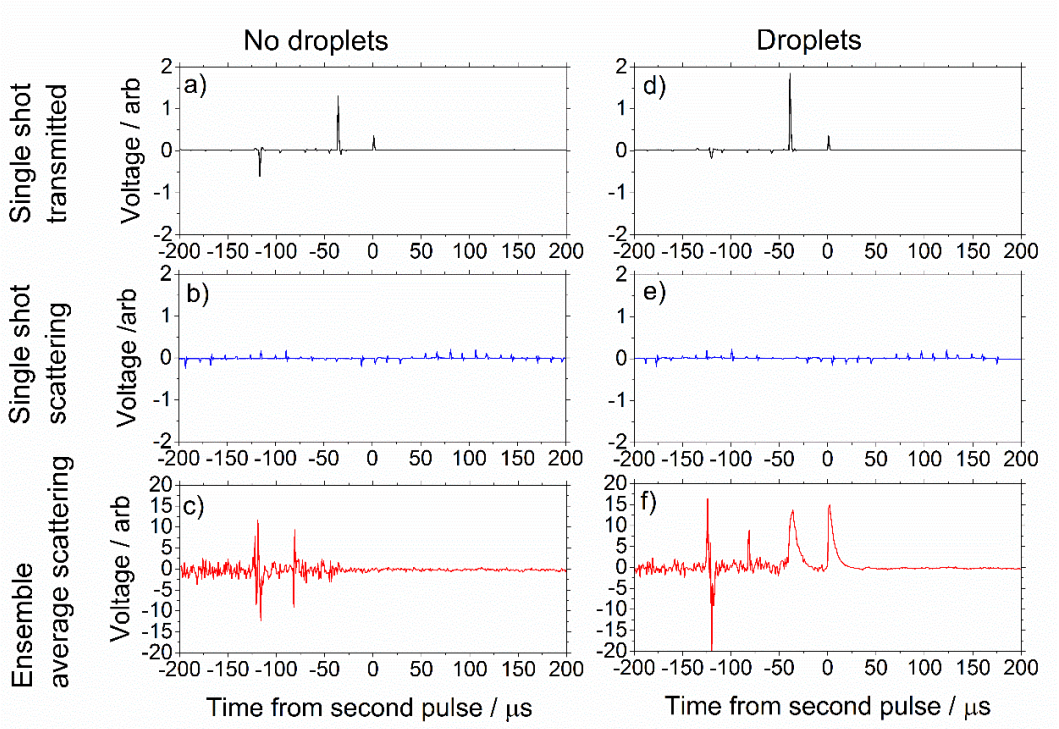

Figure 3-7 Scattered Light and Reflected Light Intensity at 45°a) Single shot transmitted light without droplets b) single shot reflected light c) summed up reflected light from 1000 experiments of the same setup d) single transmitted light with droplets e) single shot scattered light f) summed up scattered light from 1000 experiments of the same setup

Figure 3-8 shows the average normalized scattering intensity with background reflection subtracted at different angular locations. All curves are normalized at 45º to compare the relative scattering intensities among each angular positions. The experimental result can be reasonably well fitted into a Mie scattering curve calculated by the MiePlot[88] software (Version 4503) with parameters of water droplets of average diameter ~0.100 μm and sizes following a normal

distribution. This average diameter of water droplets is in the range of some published results.[47, 48] Curves of average droplet diameters of 0.200 μm were also plotted in Figure 3-8 for comparison.

However, in the future experiments, 6000 experiments are far more than required to get statistical satisfactory result. To determine the minimum number of experiments with scattering signal required at each angular location, a Monte Carlo style analysis is performed. Random samples with size from 10 to 1300 with an increment of 100 (except for the first one is 90) are randomly drawn from the group of 1000 experiments, and the statistics of each Monte Carlo simulation are calculated. This simulation has been repeated 1000 times to gain enough statistical confidence and the result is listed in Table 3.1. The peak value is defined as the integration of the scattering signal starting from its departure from the baseline and ending at the signal level coming back to the baseline. To eliminate effects of back ground signals, the background intensity is also calculated to be subtracted from the total peak integration, where the background area is defined as a time window with the same width as the peak window and 60 μs after the start time of the peak window. In order to calculate a scattering peak intensity with a 3σ confidence, 1000 experiments instead of 6000 experiments is actually needed, and this takes ~67 min if the shock tube runs at 0.25 Hz. This gives a signal to noise ratio of 15.7, which is ideal for calculating soot particles size. Another thing should be noticed is the steam jet as a particle source is usable but not steady enough. So 5000 of experiments are taken just to investigate the variation due to instability in the steam jet. However, the molecular beam from the shock tube is much more stable than the steam jet and thus much fewer experiments are expected than the steam experiments. These trials and mathematical analysis are low-cost in both time and money, thus is a good preparation for the scattering experiments with soot generated from shock tube.

Table 3-2 Monte Carlo Analysis of the Steam Experiment

# of Expts	Peak summation	BG summation	Net peak summation	Scattering per experiment	Noise level	S/N
10	5.294	0.295	5.000	0.500	0.224	2.236
100	32.840	1.092	31.749	0.317	0.056	5.635
200	59.023	1.554	57.468	0.287	0.038	7.581
300	84.256	1.918	82.337	0.274	0.030	9.074
400	109.015	2.243	106.772	0.267	0.026	10.333
500	132.572	2.443	130.129	0.260	0.023	11.407
600	156.245	2.733	153.513	0.256	0.021	12.390
700	179.548	2.905	176.643	0.252	0.019	13.291
800	202.256	3.117	199.139	0.249	0.018	14.112
900	225.800	3.331	222.468	0.247	0.017	14.915
1000	249.479	3.471	246.008	0.246	0.016	15.685
1100	271.690	3.630	268.060	0.244	0.015	16.373
1200	294.340	3.766	290.574	0.242	0.014	17.046
1300	319.121	3.959	315.161	0.242	0.014	17.753

*Peak summation: Summation of the integration of scattering signal peaks.
BG summation: Summation of the integration of background.
Net peak summation: Peak summation- BG summation.
Scattering per experiment: Net peak summation / # of experiments.
Noise level: $\frac{\sqrt{\text{Peak summation}}}{\#\text{ of experiments}}$, which is the shot noise.
S/N: Signal noise level.

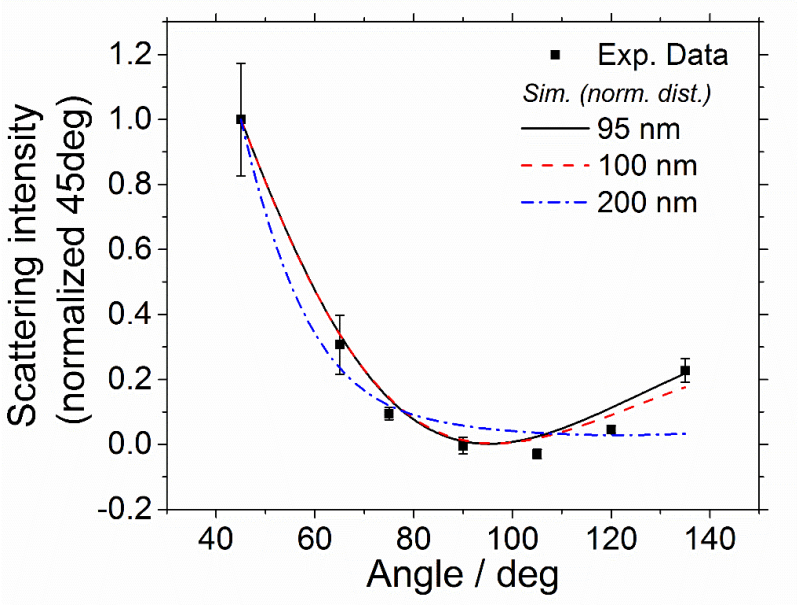

Figure 3-8 Normalized Scattering Transmitted Ratio at Different Angular Locations

3.2.5 Measured Scattered Laser Intensity and Curve Fit

Experiments are conducted at T_5 = ~1450K, ~1560K and ~1940K respectively. Driver gas is Helium (Purity Plus Gases, 99.997%). Reagent mixtures of 2% Acetone (Sigma-Aldrich, 99.9%) dilute in Argon (Purity Plus Gases, 99.9995%) are prepared from a bubbler chilled at proper temperature. A catch pot is used right after the bubbler outlet to catch spilled acetone droplets. There's a 15 dm^3 stainless steel pressure vessel used in front of shock tube driven section fill valve to stabilize the inlet gas pressure.

Around 300-600 experiments are conducted at each angular location per post shock temperature. The incident times of the laser pulses relative to the shock arrival time are binned into 10 bins as the example histogram shown in Figure 3-9. There are some amount of laser shooting before the arrival of shock waves (i.e., the relative kinetic time is negative) and the negative kinetic time bins can be found in Figure 3-10, 11, 13,14, 15 and 16. As the size of soot particles changes with kinetic time, different scattering intensities are expected to be measured at the same angular position.

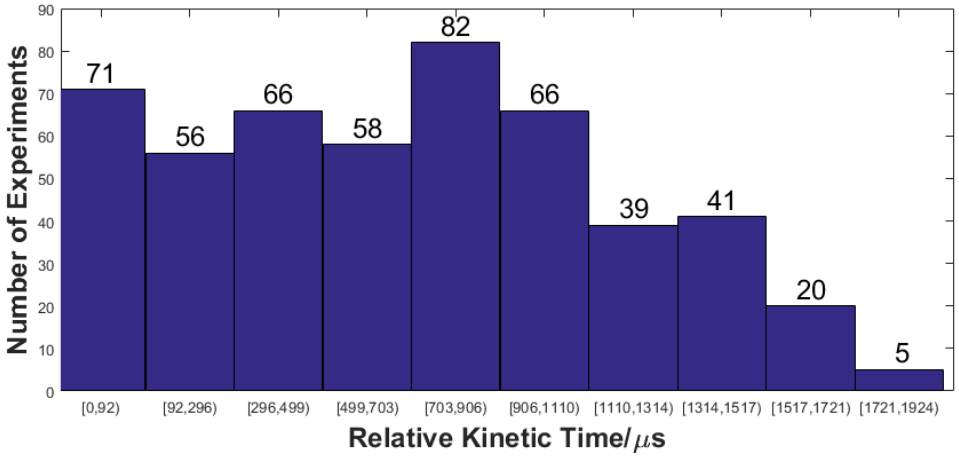

Figure 3-9 Example Kinetic Time Bins at T_5 = 1477K, Scattering Angle = 135°

3.2.5.1 Result at T_5 = 1560K

The post shock temperature T_5 is important in the soot experiment. If the temperature is too low, very few soot will form. However, if the temperature is too high, too much soot will form and

condense near the endwall area and onto the nozzle. If soot accumulates onto the nozzle, it may clog the nozzle or more seriously the molecular beam will be a mixture of soot generated at all kinetic time ranges and the kinetic time resolution is lost. T_5 = ~1560K is an appropriate post shock temperature. Results of experiments at T_5 = 1560K are presented below.

Figure 3-10 is the kinetic-time binned normalized time profiles of scattering signals at 1560K, 135°. The bins with kinetic time smaller than -550 μs and larger than 1700 μs are due to shock tube control software malfunction thus are excluded from the results. The averaged background signal is also plotted at the back of the waterfall plot for reference. It is seen from Figure 3-10 that from kinetic time -550 μs to 1025 μs, the scattering signal are all similar to the averaged background signal, which indicates very few soot can be seen within this kinetic time range. The profiles of kinetic time from 1250 μs to 1700 μs look significantly different from the background signal and also look different from each other, which indicates particles are detected within the time range and the size of particles changes with the kinetic time. The kinetic-time binned result is also quantified by integrating the scattering peak in Figure 3-11. The transmitted light intensities which represent the intensity of the laser source are also presented in the figure. The laser source intensity is relatively stable though some variations are still perceivable. Meanwhile, the background signal measured on the photomultiplier tube is also not negligible and for some kinetic time bins the scattering signal is even lower than the average background level, which means the scattering intensity at that angle within the specific kinetic time bin is near zero. To eliminate the effect of the variation in laser source intensity and background signal level on the accuracy of scattering intensity, the averaged background signal level is subtracted from the scattering signal integration to calculate the pure scattering intensity, and the ratio between the scattering and transmitted light intensity is used instead of the scattering intensity itself to fit the Mie scattering

curve.

After the background signal level is subtracted from the scattering signal measured at different angular locations, the pure scattering intensities are fitted to Mie scattering curves to estimate a distribution of the soot particle size. Figure 3-12 is the curve fit of normalized scattering intensity at T_5 = 1560K. In the kinetic time range [1250, 1475) μs, the particle diameter can be well fitted to the Mie scattering curve of 125 nm and 145 nm. In the kinetic time range [1475, 1700) μs, the particle diameter can be fitted roughly to the Mie scattering curve of 200 nm and 300 nm. The lower accuracy of the particle size is because the normalized scattering intensity is not as sensitive to the particle size in the 200-300 nm range as it is in the 100-200 nm range. However, we can still see the soot particle size is increasing with kinetic time, which is reasonable. It also should be noticed on Figure 3-11 that in the kinetic time range [1025, 1250) μs, the scattering intensity is between the intensity of [1250, 1475) μs and [1475, 1700) μs. If this signal is correct, it means the soot particle size of kinetic time range [1025, 1250) μs is between the particle size of kinetic time range [1250, 1475) μs and [1475, 1700) μs. However, if the time profile of the range [1025, 1250) μs on Figure 3-10 is compared with both the background signal, [1250, 1475) μs and [1475, 1700) μs signal, it is obvious that the [1025, 1250) μs resembles the background signal time profile much more than the [1250, 1475) μs and [1475, 1700) μs profiles. This comparison can safely rule out the [1025, 1250) μs time range from getting useful particle size information using scattering curve fit. The most possible reason for the scattering intensity detected by the PMT is between the time-of-arrival sensor detecting the shock arrival and the soot molecular beam coming across the laser beam there are several steps, like temperature rising time, soot formation time, travel time of the soot particles through the nozzle etc, thus if the time delay is ~1100 μs in the specific experiment, the time bin [1025, 1250) μs will in some shots detect the arrival of the soot particles but in most

shots does not, so the averaged scattering intensity is between the intensities of [1250, 1475) μs and [1475, 1700) μs.

There are ~15 experiments falling into the kinetic time bins [1250, 1475) μs and [1475, 1700) μs at post shock temperature T_5 = 1560K, which is fewer than the typical amount of experiments in other kinetic time bins (~40-50 experiments per bin). Fewer experiments in the kinetic time bins results in higher noise levels in the two bins, which is also illustrated by noisier base lines of the time profiles of the two scattering signal as shown in Figure 3-10. However, the signal to noise levels of the two interesting bins are still usable compared to their signal levels. The noise levels of kinetic time bins [1250, 1475) μs and [1475, 1700) μs are represented as error bars on Figure 3-11. The error bars of the two kinetic time bins are neither comparable to the raw scattering signal nor to the pure scattering signal (raw scattering signal – background signal level). Also the lower bounds of the error bars of each of the two kinetic time bins are much higher than the background signal level, so the particle sizes calculated using the scattering signals of the two kinetic time bins are still reliable. However, if the control algorithm of the shock tube can be improved to adapt the time delay mentioned in the previous paragraph, more experiments will fall into the more interesting kinetic time bins and a lower noise level can be expected.

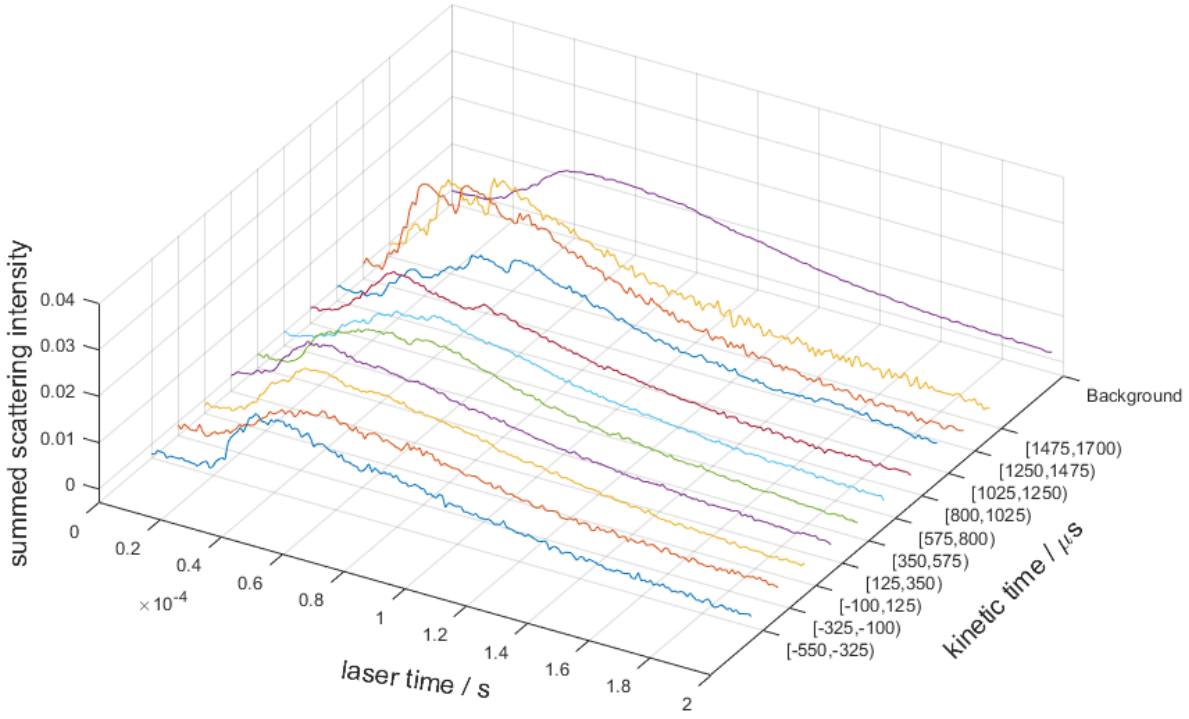

Figure 3-10 Kinetic-time Binned Time Profiles of Scattering Signals, T_5 = 1560K, Scattering Angle = 135°

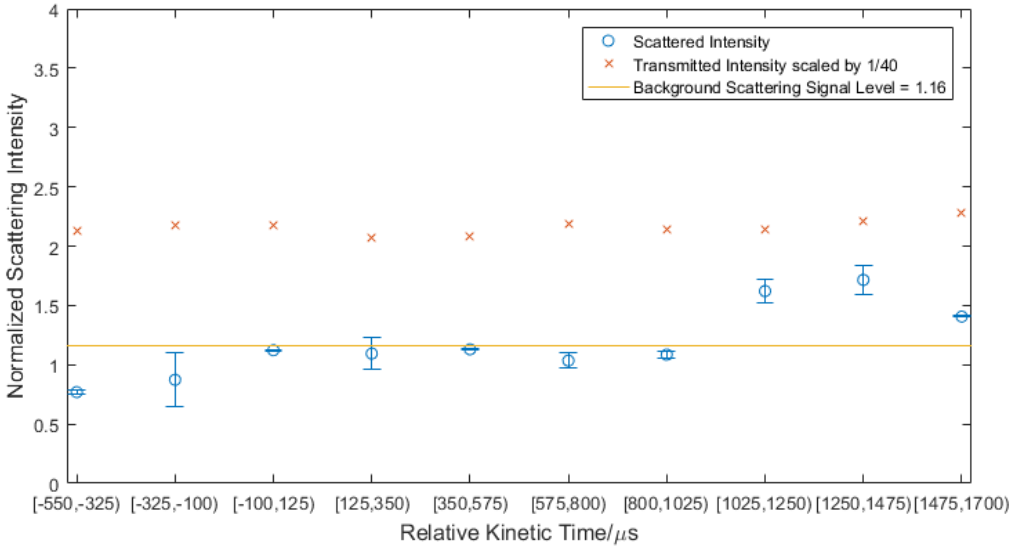

Figure 3-11 Normalized Scattering Intensity at Different Kinetic Time, T5 = 1560K, Scattering Angle = 115°

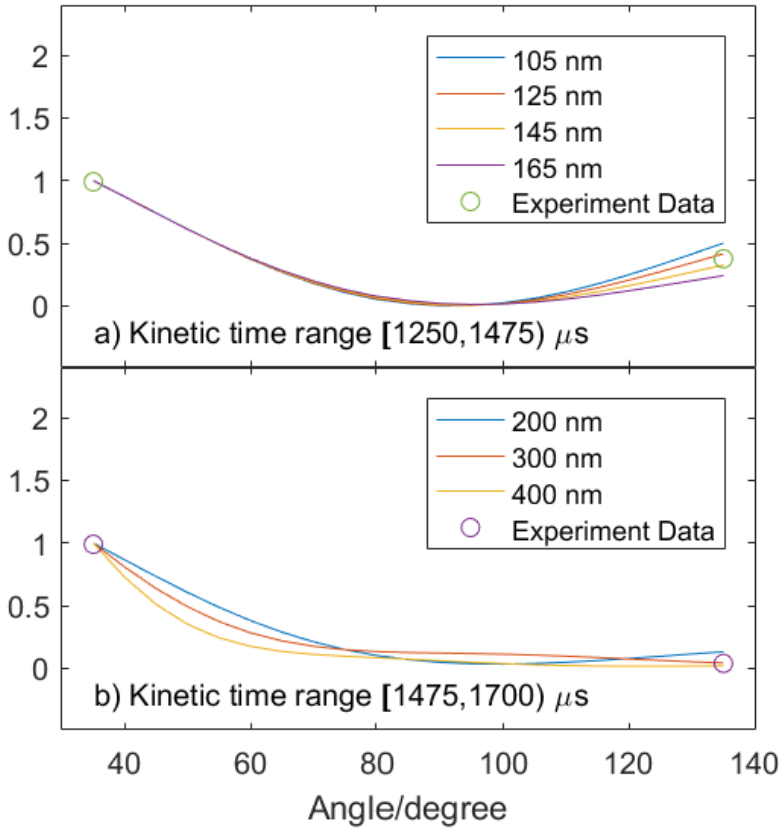

Figure 3-12 Mie Scattering Curve Fit at 1560K a) Kinetic time range between 1250 μs and 1475 μs. b) Kinetic time range between 1475 μs and 1700 μs.

3.2.5.2 Result at T_5 = 1940K

Figure 3-13 is the kinetic-time binned normalized time profiles of scattering signals at 1940K, 115°. The time profiles are not evenly spaced because no experiments falling into some bins so the summed results of those bins are not shown. The kinetic-time binned result is also quantified by integrating the scattering peak in Figure 3-14. It is seen from Figure 3-13 that in the range [-550, -325) μs, [-325, -100) μs and [1475,1700) μs, the noise level is much larger than other bins. This is because within these time ranges there are much fewer experiments than other bins, thus the data from the 3 bins are not reliable and should be excluded from analysis. All other time profiles, though have much lower noise level, resemble each other in the shape and are similar with the

background signal profile, especially the two most interesting kinetic time bins, [1250, 1475) μs and [1475,1700) μs, not only look very similar in the time profile, but also has the very close scattering intensity as shown on the Figure 3-14. This indicates at the T5 as high as ~1940K, there is already soot condensed on to the nozzle so the particle in the molecular beam can be from any previous cycles and the kinetic time resolution is lost. Therefore, it is meaningless to fit the scattering signals and solve for the particle size.

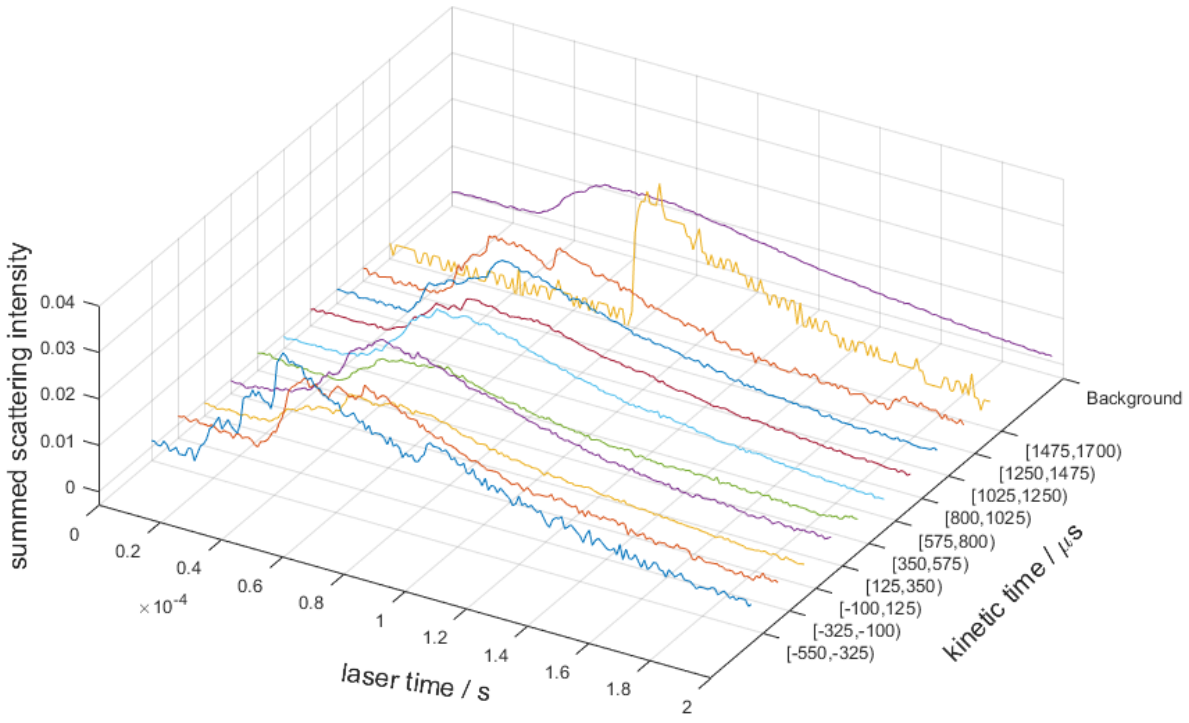

Figure 3-13 Kinetic-time Binned Time Profiles of Scattering Signals, T_5 = 1940K, Scattering Angle = 115°

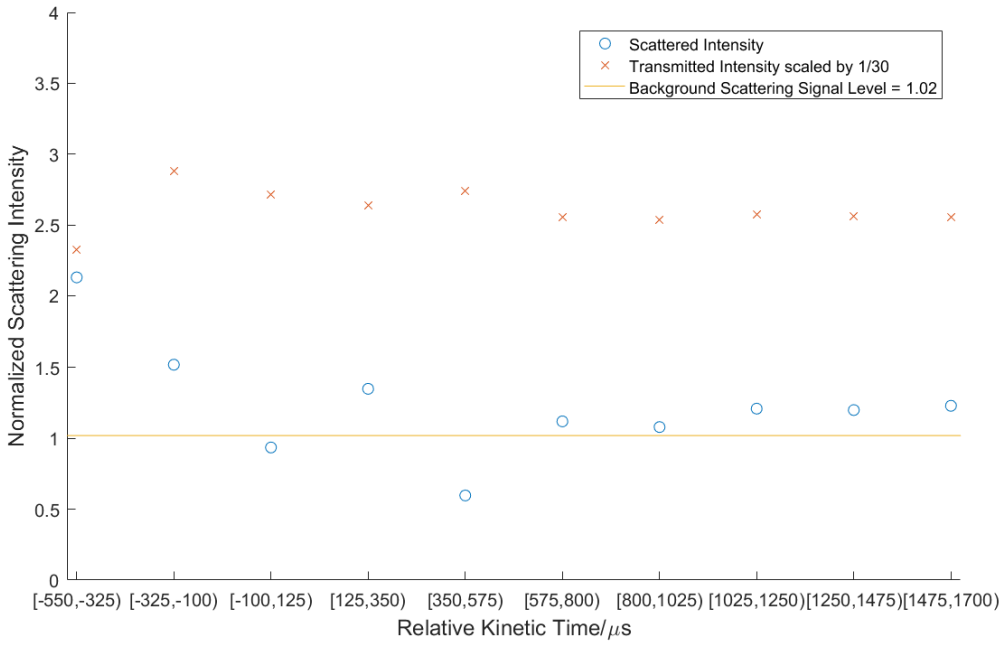

Figure 3-14 Scattering Intensity at Different Kinetic Time, T_5 = 1940K, Scattering Angle = 115°

3.2.5.3 Result at T_5 = 1450K

Unlike the experiment result at T_5 = 1940K and 1560K, the variations of the scattering light intensity at T_5 = 1450K among different kinetic time bins are much smaller as shown in Figure 3-15. The shape and height of the scattering signal peaks at different kinetic times are similar to each other. The less variations among different kinetic times are also well presented in the peak integrations shown in Figure 3-16. This indicates at T_5 = 1450K, almost no soot is formed, thus the molecular beam coming across with the laser beam consists almost no particles.

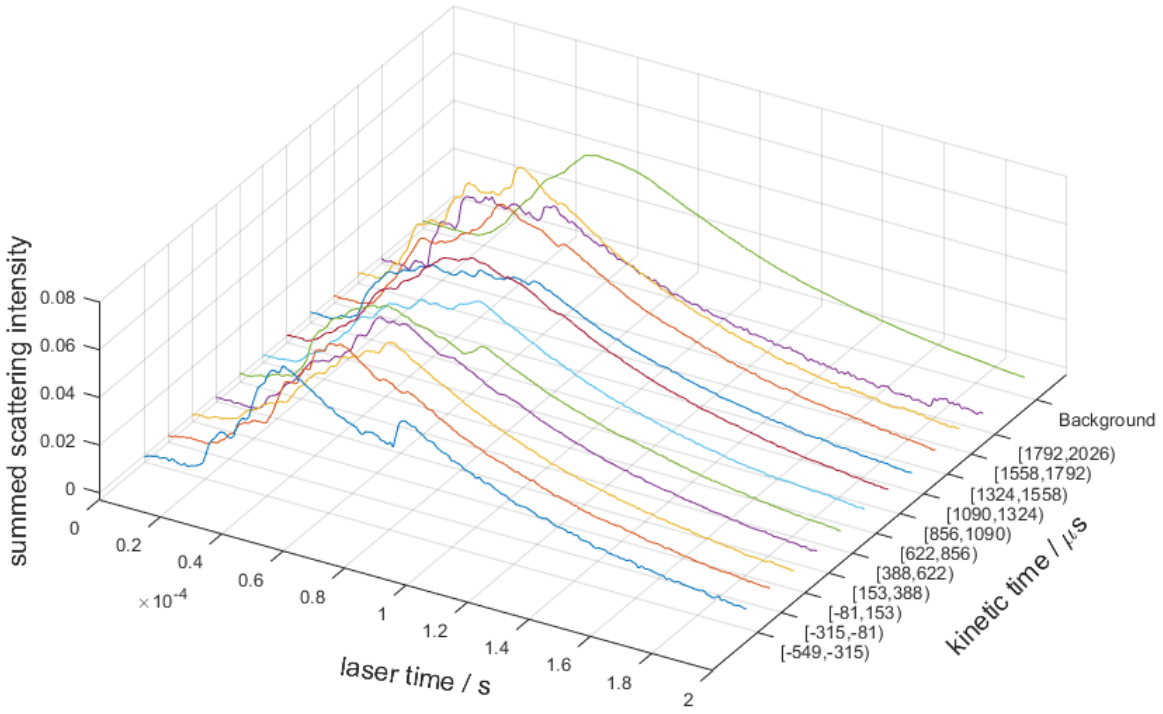

Figure 3-15 Kinetic-time Binned Time Profiles of Scattering Signals, T_5 = 1450K, Scattering Angle = 135°

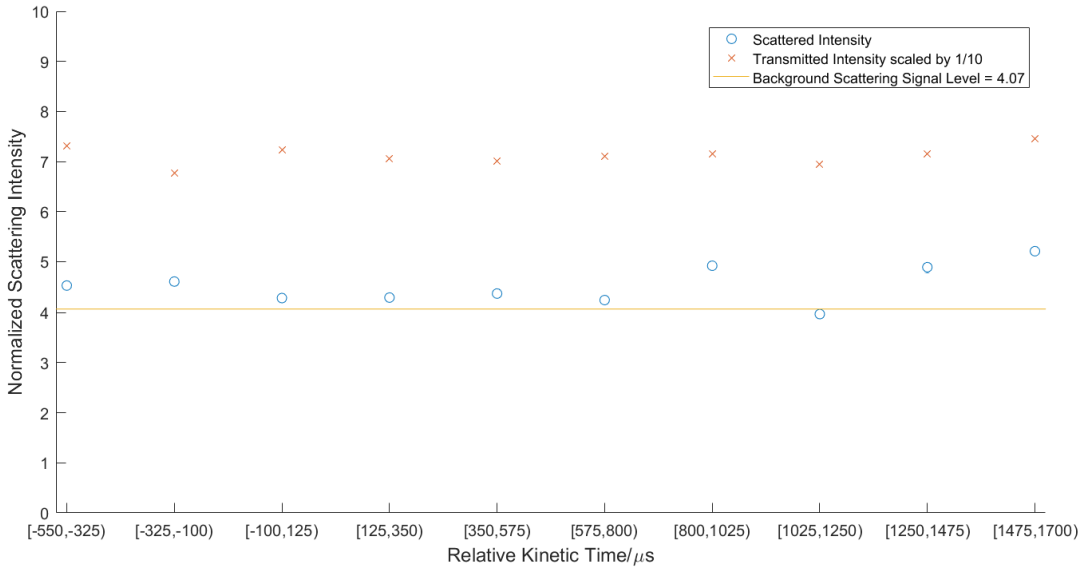

Figure 3-16 Normalized Scattering Intensity at Different Kinetic Time, T_5 = 1450K, Scattering Angle = 135°

Chapter 4. Summary, Conclusion and Future Work

4.1 Summary and Conclusion

In this research project, two experiments are conducted with the motivation of supplementing study of soot formation mechanisms in high pressure combustion:

a) Using synchrotron sourced PIMS to measure soot related species and concentration in the intermediate species phase and particle matter phase of a miniature engine.

b) Use laser scattering techniques to measure size of soot generated in a shock tube in the particle matter phase

Experimental setups of the two experiments are presented and results are discussed.

In the miniature engine experiments, a mobile engine measurement bench suitable for in-laboratory experiment is developed at UM-Dearborn and taken to the Advanced Light Source to measure in-cylinder and exhaust species and concentrations using Synchrotron sourced PIMS. A customer made engine cylinder head with a small sampling nozzle is made in order to sample directly from the high pressure environment in the combustion chamber to the molecular beam machine. Experiments are conducted at different engine speed ranges and castor oil concentration in the fuel. Samples of in-cylinder and exhaust gas are both taken to the PIMS to analyze species and measure concentrations. Mass spectra and PIE curves of the samples at different experiment conditions and sampling locations are obtained. Species of different mass charge ratios are identified clearly with their relative concentration on the mass spectra. Isomers and different species with the same mass charge ratio are resolved by observing the ionization energy on the PIE curve. This set of engine-PIMS experiments proves the effectiveness of the experimental

design and presents a way to extend the usage of PIMS to higher combustion conditions.

However, the current design also has several drawbacks:

a) Using a long sampling line to connect between the sampling nozzle on the cylinder head and the molecular beam machine entrance. The sampling line renders loss of most radicals so the measurement of species is time-averaged instead of time-resolved.
b) The engine displacement is too small. The small volume of the combustion chamber limits the size of the sampling orifice, which lowers the signal noise ratio.

Suggestions on future experiments are given in next section to solve the problems encountered.

In the shock tube soot experiment, soot particles are generated in well-controlled conditions from the High Repetition Rate Shock Tube at UM-Dearborn. The soot generated inside the shock tube is sampled into a vacuum chamber in the form of a molecular beam and the soot particle size is measured using laser scattering techniques. The sampling chamber and the optical system are designed and developed. The optical system is also validated by measuring steam clusters to verify the signal to noise level and reduce unnecessary experiments before working on measuring soot particles. The experiments are conducted at three different post-shock temperatures and only T_5 = 1560K falls into the appropriate temperature range to be high enough to generate soot while to not generate too much soot and condensing onto the sampling nozzle. The scattering intensities at two different angular locations at different kinetic times are fitted to Mie scattering curves respectively and a set of reasonable particles sizes is acquired for each kinetic time.

The shock tube experiments suffer from relatively low signal noise levels although some methods have already been applied to improve the S/N as discussed in Chapter 2 and 3. Future experiments can do directly in-situ measurement near the shock tube endwall. Some suggestions are given in Section 4.2.

4.2 Future Work

In future engine-PIMS experiments, the engine should be directly connected to the entrance of the molecular beam machine. The direct coupling has three benefits:

1) Very little time delay exists between gas sample exiting the combustion chamber and entering into the molecular beam machine. Thus a measurement of species concentrations with high time resolution can be obtained, which is fundamental to developing accurate kinetics models.
2) Directly connecting the cylinder head nozzle and molecular beam machine can result in higher signal level and accordingly high signal to noise ratios.
3) Much less radicals are combined on their way to the PIMS thus more radicals can be seen on the mass spectrum. This is also very important in developing high-accuracy kinetics model.

The engine used in this pilot experiment is a model airplane engine which has a 10 cc displacement. This is a pretty conservative design in order to fit the in-lab measurement environment. The small volume severely limits the nozzle size used in the cylinder head, because too large of the orifice will lower the combustion chamber pressure too much and cause the engine not to run self-sustainable. In practice it is assured that a tens of times larger engine is still feasible for indoor measurement application, as long as noise dumping, ventilation, heat radiation etc. are well designed. So in the future experiments, a lawn mower engine can be used and this is a straightforward way to improve the signal noise ratio by tens of times.

In future shock tube experiments, some in-situ scattering measurement of soot can be conducted. The in-situ scattering measurement can be done with a customized transparent end section, or a metal end section with adaption ports for optical access at different angular locations. The improvement is demonstrated in Figure 4-1.

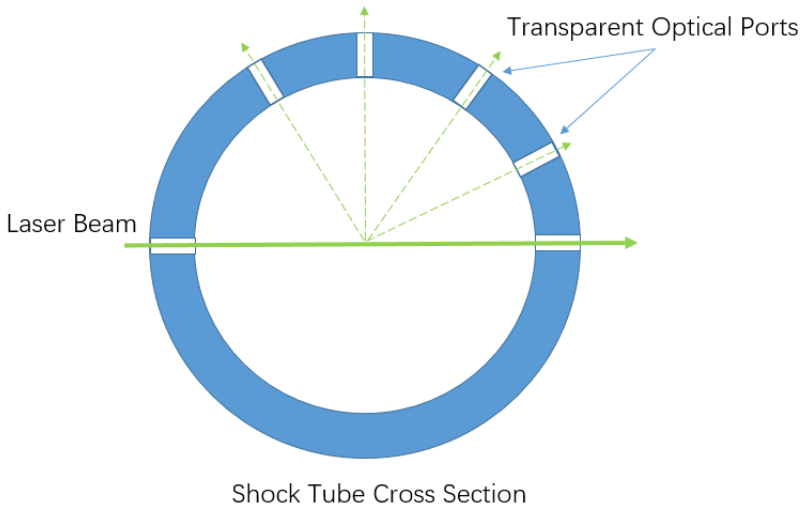

Figure 4-1 Demonstration Schematic of in-situ Measurement of Soot

Reference

[1] J. J. Ivie and L. J. Forney, "A numerical model of the synthesis of carbon black by benzene pyrolysis," *AIChE J.*, vol. 34, no. 11, pp. 1813–1820, 1988.

[2] Z. Y. Zhou, Z. Z. Huang, D. J. Chen, Q. Wang, N. Tian, and S. G. Sun, "High-index faceted platinum nanocrystals supported on carbon black as highly efficient catalysts for ethanol electrooxidation," *Angew. Chemie - Int. Ed.*, vol. 49, no. 2, pp. 411–414, 2010.

[3] C. Roy, B. Labrecque, and B. de Caumia, "Recycling of scrap tires to oil and carbon black by vacuum pyrolysis," *Resour. Conserv. Recycl.*, vol. 4, no. 3, pp. 203–213, Sep. 1990.

[4] W. Kaminsky and C. Mennerich, "Pyrolysis of synthetic tire rubber in a fluidised-bed reactor to yield 1,3-butadiene, styrene and carbon black," *J. Anal. Appl. Pyrolysis*, vol. 58–59, pp. 803–811, 2001.

[5] I. Glassman and R. A. Yetter, *Combustion*. Elsevier, 2008.

[6] B. S. Haynes and H. G. Wagner, "Soot Formation," *Prog. Energy Combust. Sci.*, vol. 7, no. 4, pp. 229–273, 1981.

[7] I. M. Kennedy, "The health effects of combustion-generated aerosols," *Proc. Combust. Inst.*, vol. 31 II, pp. 2757–2770, 2007.

[8] M. Shiraiwa, K. Selzle, and U. Pöschl, "Hazardous components and health effects of atmospheric aerosol particles: reactive oxygen species, soot, polycyclic aromatic compounds and allergenic proteins," *Free Radic. Res.*, vol. 46, no. 8, pp. 927–939, 2012.

[9] "Emission Standards." [Online]. Available: https://www.dieselnet.com/standards/us/hd.php#sum.

[10] I. Glassman and R. A. Yetter, *Combustion*. Elsevier, 2008.

[11] M. Kobayashi, R. Imai, and O. Fujita, "Comparison of soot formation characteristics between DME diffusion flame and the partially premixed methane flame," *Trans. Japan Soc. Mech. Eng.*, vol. 74, no. 12, pp. 2718–2723, 2008.

[12] H. S. Zhen, C. W. Leung, and C. S. Cheung, "A comparison of the heat transfer behaviors of biogas-H2 diffusion and premixed flames," *Int. J. Hydrogen Energy*, vol. 39, no. 2, pp. 1137–1144, 2014.

[13] X. Mercier, E. Therssen, J. . Pauwels, and P. Desgroux, "Cavity ring-down measurements of OH radical in atmospheric premixed and diffusion flames.," *Chem. Phys. Lett.*, vol. 299, no. 1, pp. 75–83, 1999.

[14] R. Isermann, *Engine Modeling and Control*. 2014.

[15] D. R. Tree and K. I. Svensson, "Soot processes in compression ignition engines," *Prog. Energy Combust. Sci.*, vol. 33, no. 3, pp. 272–309, 2007.

[16] O. Salvat, P. Marez, and G. Belot, "Passenger Car Serial Application of a Particulate Filter System on a Common Rail Direct Injection Diesel Engine," vol. 2000, no. 724, 2000.

[17] P. Soltic, D. Edenhauser, T. Thurnheer, D. Schreiber, and A. Sankowski, "Experimental investigation of mineral diesel fuel, GTL fuel, RME and neat soybean and rapeseed oil combustion in a heavy duty on-road engine with exhaust gas aftertreatment," *Fuel*, vol. 88, no. 1, pp. 1–8, 2009.

[18] H. Richter and J. . Howard, *Formation of polycyclic aromatic hydrocarbons and their growth to soot—a review of chemical reaction pathways*, vol. 26, no. 4–6. 2000.
[19] C. J. Pope and J. a. Miller, "Exploring old and new benzene formation pathways in lowpressure premixed flames of aliphatic fuels," *Proc. Combust. Inst.*, vol. 28, no. 2, pp. 1519–1527, 2000.
[20] H. Anderson, C. S. McEnally, and L. D. Pfefferle, "Experimental study of naphthalene formation pathways in non-premixed methane flames doped with alkylbenzenes," *Proc. Combust. Inst.*, vol. 28, no. 2, pp. 2577–2583, 2000.
[21] M. Frenklach, D. W. Clary, W. C. Gardiner, and S. E. Stein, "Detailed kinetic modeling of soot formation in shock-tube pyrolysis of acetylene," *Symp. Combust.*, vol. 20, no. 1, pp. 887–901, 1985.
[22] J. D. Bittner and J. B. Howard, "Composition profiles and reaction mechanisms in a near-sooting premixed benzene/oxygen/argon flame," *Symp. Combust.*, vol. 18, no. 1, pp. 1105–1116, 1981.
[23] M. Frenklach and H. Wang, "Detailed modeling of soot particle nucleation and growth," *Symp. Combust.*, vol. 23, no. 1, pp. 1559–1566, Jan. 1991.
[24] N. W. Moriarty, N. J. Brown, and M. Frenklach, "Hydrogen migration in the phenylethen-2-yl radical," *J. Phys. Chem. A*, vol. 103, no. 35, pp. 7127–7135, 1999.
[25] H. Wang and M. Frenklach, "Calculations of Rate Coefficients for the Chemically Activated Reactions of Acetylene with Vinylic and Aromatic Radicals," *J. Phys. Chem.*, vol. 98, no. 44, pp. 11465–11489, 1994.
[26] D. S. N. Parker, R. I. Kaiser, T. P. Troy, and M. Ahmed, "Hydrogen abstraction/acetylene addition revealed.," *Angew. Chem. Int. Ed. Engl.*, vol. 53, no. 30, pp. 7740–4, Jul. 2014.
[27] M. MUSICK, P. J. VAN TIGGELEN, and J. VANDOOREN, "Flame Structure Studies of Several Premixed Ethylene - Oxygen - Argon Flames at Equivalence Ratios from 1.00 to 2.00," *Combust. Sci. Technol.*, vol. 153, no. 1, pp. 247–261, Apr. 2000.
[28] C. Renard, V. Dias, P. J. Van Tiggelen, and J. Vandooren, "Flame structure studies of rich ethylene-oxygen-argon mixtures doped with CO2, or with NH3, or with H2O," *Proc. Combust. Inst.*, vol. 32 I, no. 1, pp. 631–637, 2009.
[29] M. Balthasar and M. Kraft, "A stochastic approach to calculate the particle size distribution function of soot particles in laminar premixed flames," *Combust. Flame*, vol. 133, no. 3, pp. 289–298, 2003.
[30] Y. D. Zhang, S. Li, and C. Lou, "Dynamics simulation and reaction pathway analysis of characteristics of soot particles in ethylene oxidation at high temperature," *Russ. J. Appl. Chem.*, vol. 87, no. 4, pp. 525–535, 2014.
[31] R. I. A. Patterson, J. Singh, M. Balthasar, M. Kraft, and W. Wagner, "Extending stochastic soot simulation to higher pressures," *Combust. Flame*, vol. 145, no. 3, pp. 638–642, 2006.
[32] E. S. Abdrakhimova and V. Z. Abdrakhimov, "Study of combustion processes in firing of a heat-insulator produced from technogenic raw materials from nonferrous metallurgy and power industry," *Russ. J. Appl. Chem.*, vol. 85, no. 8, pp. 1186–1191, 2012.
[33] F. Roper, C. Smith, and I. Fells, "A scanning optical densitometer using deconvolution to measure soot concentrations in axisymmetric flames," *J. Phys. E Sci. ...*, vol. 15, pp. 1177–1183, 1982.
[34] M. Leschowski, K. A. Thomson, D. R. Snelling, C. Schulz, and G. J. Smallwood, "Combination of LII and extinction measurements for determination of soot volume

fraction and estimation of soot maturity in non-premixed laminar flames," *Appl. Phys. B Lasers Opt.*, vol. 119, no. 4, pp. 685–696, 2015.
[35] P. T. Lynch, T. P. Troy, M. Ahmed, and R. S. Tranter, "Probing Combustion Chemistry in a Miniature Shock Tube with Synchrotron VUV Photo Ionization Mass Spectrometry," *Anal. Chem.*, vol. 87, no. 4, pp. 2345–2352, 2015.
[36] D. B. Lenhert and S. L. Manzello, "Effects of benzene and naphthalene addition on soot inception in a well-stirred reactor/plug flow reactor," *Proc. Combust. Inst.*, vol. 32 I, no. 1, pp. 657–664, 2009.
[37] S. L. Manzello, D. B. Lenhert, A. Yozgatligil, M. T. Donovan, G. W. Mulholland, M. R. Zachariah, and W. Tsang, "Soot particle size distributions in a well-stirred reactor / plug flow reactor," vol. 31, pp. 675–683, 2007.
[38] C. P. Rüger, M. Sklorz, T. Schwemer, and R. Zimmermann, "Characterisation of ship diesel primary particulate matter at the molecular level by means of ultra-high-resolution mass spectrometry coupled to laser desorption ionisation - Comparison of feed fuel, filter extracts and direct particle measurements," *Anal. Bioanal. Chem.*, vol. 407, no. 20, pp. 5923–5937, 2015.
[39] J. Kim, E. Yim, C. Jeon, C. Jung, and B. Han, "Cold performance of various biodiesel fuel blends at low temperature," *Int. J. ...*, vol. 13, no. 2, pp. 293–300, 2012.
[40] S. Jiménez, J. Barroso, A. Pina, and J. Ballester, "Size distribution and concentration of soot generated in oil and gas-fired residential boilers under different combustion conditions," *Atmos. Environ.*, vol. 133, pp. 60–67, 2016.
[41] J. Reimann, S. A. Kuhlmann, and S. Will, "Improvement in soot concentration measurements by laser-induced incandescence (LII) through a particle size correction," *Combust. Flame*, vol. 153, no. 4, pp. 650–654, 2008.
[42] C. A. Taatjes, N. Hansen, A. McIlroy, J. A. Miller, J. P. Senosiain, S. J. Klippenstein, F. Qi, L. Sheng, Y. Zhang, T. A. Cool, J. Wang, P. R. Westmoreland, M. E. Law, T. Kasper, and K. Kohse-Höinghaus, "Enols are common intermediates in hydrocarbon oxidation.," *Science (80-.).*, vol. 308, no. 5730, pp. 1887–9, Jun. 2005.
[43] N. Hansen, T. A. Cool, P. R. Westmoreland, and K. Kohse-Höinghaus, "Recent contributions of flame-sampling molecular-beam mass spectrometry to a fundamental understanding of combustion chemistry," *Prog. Energy Combust. Sci.*, vol. 35, no. 2, pp. 168–191, Apr. 2009.
[44] F. Qi, "Combustion chemistry probed by synchrotron VUV photoionization mass spectrometry," *Proc. Combust. Inst.*, vol. 34, no. 1, pp. 33–63, Jan. 2013.
[45] B. Yang, Y. Li, L. Wei, C. Huang, J. Wang, Z. Tian, R. Yang, L. Sheng, Y. Zhang, and F. Qi, "An experimental study of the premixed benzene/oxygen/argon flame with tunable synchrotron photoionization," *Proc. Combust. Inst.*, vol. 31, no. 1, pp. 555–563, Jan. 2007.
[46] D. L. Osborn, P. Zou, H. Johnsen, C. C. Hayden, C. A. Taatjes, V. D. Knyazev, S. W. North, D. S. Peterka, M. Ahmed, and S. R. Leone, "The multiplexed chemical kinetic photoionization mass spectrometer: a new approach to isomer-resolved chemical kinetics.," *Rev. Sci. Instrum.*, vol. 79, no. 10, p. 104103, Oct. 2008.
[47] A. Vasiliou, K. M. Piech, X. Zhang, M. R. Nimlos, M. Ahmed, A. Golan, O. Kostko, D. L. Osborn, J. W. Daily, J. F. Stanton, and G. B. Ellison, "The products of the thermal decomposition of CH3CHO.," *J. Chem. Phys.*, vol. 135, no. 1, p. 014306, Jul. 2011.
[48] O. Herbinet, P. A. Glaude, F. B. Leclerc, and R. Fournet, "Experimental confirmation of

the low-temperature oxidation scheme of alkanes.," *Angew. Chem. Int. Ed. Engl.*, vol. 49, no. 18, pp. 3169–72, Apr. 2010.
[49] F. Battin-Leclerc, O. Herbinet, P. Glaude, R. Fournet, Z. Zhou, L. Deng, H. Guo, M. Xie, and F. Qi, "New Experimental evidences about the formation and consumption of ketohydroperoxides," *Proc. Combust. Inst.*, vol. 33, no. 1, pp. 325–331, Dec. 2011.
[50] A. J. Eskola, O. Welz, J. Zádor, I. O. Antonov, L. Sheps, J. D. Savee, D. L. Osborn, and C. A. Taatjes, "Probing the low-temperature chain-branching mechanism of n-butane autoignition chemistry via time-resolved measurements of ketohydroperoxide formation in photolytically initiated n-C4H10 oxidation," *Proc. Combust. Inst.*, vol. 35, no. 1, pp. 291–298, 2015.
[51] M. Knauer, M. E. Schuster, D. S. Su, R. Schlögl, R. Niessner, and N. P. Ivleva, "Soot structure and reactivity analysis by Raman Microspectroscopy, Temperature-Programmed Oxidation, and High-Resolution Transmission Electron Microscopy," *J. Phys. Chem. A*, vol. 113, no. 50, pp. 13871–13880, 2009.
[52] A. C. Barone, "Morphological characterization of the early process of soot formation by atomic force microscopy," *Combust. Flame*, vol. 132, no. 1–2, pp. 181–187, 2003.
[53] R. L. Vander Wal, "Soot precursor carbonization: Visualization using LIF and LII and comparison using bright and dark field TEM," *Combust. Flame*, vol. 112, no. 4, pp. 607–616, 1998.
[54] M. K. Bobba and M. P. B. Musculus, "Laser diagnostics of soot precursors in a heavy-duty diesel engine at low-temperature combustion conditions," *Combust. Flame*, vol. 159, no. 2, pp. 832–843, Feb. 2012.
[55] R. Vander Wal, "Soot Precursor Carbonization: Visualization Using LIF and LII and Comparison Using Bright and Dark Field TEM," *Combust. Flame*, vol. 112, no. 4, pp. 607–616, Mar. 1998.
[56] R. Di Sante, "Laser extinction technique for measurements of carbon particles concentration during combustion," *Opt. Lasers Eng.*, vol. 51, no. 6, pp. 783–789, 2013.
[57] B. Yang and U. O. Koylu, "Detailed soot field in a turbulent non-premixed ethylene/air flame from laser scattering and extinction experiments," *Combust. Flame*, vol. 141, no. 1–2, pp. 55–65, Apr. 2005.
[58] S. N. Foner and R. L. Hudson, "The Detection of Atoms and Free Radicals in Flames by Mass Spectrometric Techniques," *J. Chem. Phys.*, vol. 21, no. 8, p. 1374, 1953.
[59] R. Friedman and J. A. Cyphers, "Flame Structure Studies. III. Gas Sampling in a Low-Pressure Propane-Air Flame," *J. Chem. Phys.*, vol. 23, no. 10, p. 1875, 1955.
[60] C. P. Lazzara, J. C. Biordi, and J. F. Papp, "Concentration profiles for radical species in a methane-oxygen-argon flame," *Combust. Flame*, vol. 21, no. 3, pp. 371–382, Dec. 1973.
[61] a. R. P. Rau, "The Wannier theory for two electrons escaping from a positive ion," *Phys. Rep.*, vol. 110, pp. 369–387, 1984.
[62] H. Hurzeler, M. G. Inghram, and J. D. Morrison, "Photon Impact Studies of Molecules Using a Mass Spectrometer," *J. Chem. Phys.*, vol. 28, no. 1, p. 76, 1958.
[63] C. a Taatjes, N. Hansen, A. McIlroy, J. a Miller, J. P. Senosiain, S. J. Klippenstein, F. Qi, L. Sheng, Y. Zhang, T. a Cool, J. Wang, P. R. Westmoreland, M. E. Law, T. Kasper, and K. Kohse-Höinghaus, "Enols are common intermediates in hydrocarbon oxidation.," *Science*, vol. 308, no. June, pp. 1887–1889, 2005.
[64] R. I. Kaiser, P. Maksyutenko, C. Ennis, F. Zhang, X. Gu, S. P. Krishtal, A. M. Mebel, O. Kostko, and M. Ahmed, "Untangling the chemical evolution of Titan's atmosphere and

surface--from homogeneous to heterogeneous chemistry.," *Faraday Discuss.*, vol. 147, pp. 429–478; discussion 527–552, 2010.
[65] E. R. Mysak, K. R. Wilson, M. Jimenez-Cruz, M. Ahmed, and T. Baer, "Synchrotron radiation based aerosol time-of-flight mass spectrometry for organic constituents.," *Anal. Chem.*, vol. 77, no. 18, pp. 5953–60, Sep. 2005.
[66] E. R. Mysak, K. R. Wilson, M. Jimenez-cruz, M. Ahmed, T. Baer, N. Carolina, C. Hill, and C. Sciences, "Synchrotron Radiation Based Aerosol Time-of-Flight Mass Spectrometry for Organic Constituents spectrometer using tunable vacuum-ultraviolet (VUV)," vol. 77, no. 18, pp. 5953–5960, 2005.
[67] P. Liu, P. J. Ziemann, D. B. Kittelson, and P. H. McMurry, "Generating Particle Beams of Controlled Dimensions and Divergence: I. Experimental Evaluation of Particle Motion in Aerodynamic Lenses and Nozzle Expansions," *Aerosol Sci. Technol.*, vol. 22, no. 3, pp. 293–313, 1995.
[68] P. Liu, P. J. Ziemann, D. B. Kittelson, and P. H. McMurry, "Generating Particle Beams of Controlled Dimensions and Divergence: II. Experimental Evaluation of Particle Motion in Aerodynamic Lenses and Nozzle Expansions," *Aerosol Sci. Technol.*, vol. 22, no. 3, pp. 314–324, 1995.
[69] NIST, "Oxygen." [Online]. Available: http://webbook.nist.gov/cgi/cbook.cgi?ID=C7782447&Mask=20#Ion-Energetics.
[70] W. Tao, R. B. Klemm, F. L. Nesbitt, and L. J. Stief, "A Discharge Flow-Photoionization Mass-Spectrometric Study of Hydroxymethyl Radicals (H2COH and H2COD) - Photoionization Spectrum and Ionization-Energy," *J. Phys. Chem.*, vol. 96, no. 6, pp. 104–107, 1992.
[71] R. S. Tranter, K. Brezinsky, and D. Fulle, "Design of a high-pressure single pulse shock tube for chemical kinetic investigations," *Rev. Sci. Instrum.*, vol. 72, no. 7, p. 3046, 2001.
[72] A. Fridlyand, P. T. Lynch, R. S. Tranter, and K. Brezinsky, "Single pulse shock tube study of allyl radical recombination," *J. Phys. Chem. A*, vol. 117, no. 23, pp. 4762–4776, 2013.
[73] K. Yasunaga, T. Mikajiri, S. M. Sarathy, T. Koike, F. Gillespie, T. Nagy, J. M. Simmie, and H. J. Curran, "A shock tube and chemical kinetic modeling study of the pyrolysis and oxidation of butanols," *Combust. Flame*, vol. 159, no. 6, pp. 2009–2027, 2012.
[74] K. Grogan, Q. Wang, and M. Ihme, "Modeling Gas Dynamic Effects in Shock-Tubes for Reaction Kinetics Measurements," no. January, pp. 1–12, 2015.
[75] K. L. Riley, P. E. Morris, and F. Park, "SHOCK-TUBE GAS TEMPERATURE MEASUREMENTS BY INFRARED MONOCHROMATIC RADIATION PYROMETRY," pp. 1–4, 1993.
[76] R. S. Tranter and P. T. Lynch, "A miniature high repetition rate shock tube," *Rev. Sci. Instrum.*, vol. 84, no. 9, 2013.
[77] P. T. Lynch and G. Wang, "Chemical thermometry in miniature HRRST using 1,1,1-trifluoroethane dissociation," *Proc. Combust. Inst.*, vol. 000, pp. 1–8, 2016.
[78] H. C. van de Hulst, *Light scattering by small particles*. 2012.
[79] E. Hecht, *Optics*, 4th ed. Pearson/Addison Wesley, 2002.
[80] B.-N. Akiva, *Shock Waves in Chemistry*. New York: MARCEL DEKKER, INC., 1981.
[81] A. G. Gaydon and I.R.Hurle, *The Shock Tube in High Temperature Chemical and Physics*. New York: Reinhold Publishing Corporation, 1963.
[82] O. Kostko, L. Belau, K. R. Wilson, and M. Ahmed, "Vacuum-ultraviolet (VUV) photoionization of small methanol and methanol-water cluster," *J. Phys. Chem. A*, vol.

112, no. 39, pp. 9555–9562, 2008.
[83] Y.-R. Luo and P. D. Pacey, “Effects of alkyl substitution on ionization energies of alkanes and haloalkanes and on heats of formation of their molecular cations Part 2.* Alkanes and chloro-, bromo- and iodoalkanes,” *Int. J. Mass Spectrom. Ion Process.*, vol. 112, no. 1, pp. 63–77, Jan. 1992.
[84] J. C. Traeger, “Heat of formation for the formyl cation by photoionization mass spectrometry,” *Int. J. Mass Spectrom. Ion Process.*, vol. 66, no. 3, pp. 271–282, Jun. 1985.
[85] K. Müller-Dethlefs, M. Sander, and E. W. Schlag, “Two-colour photoionization resonance spectroscopy of NO: Complete separation of rotational levels of NO+ at the ionization threshold,” *Chem. Phys. Lett.*, vol. 112, no. 4, pp. 291–294, Dec. 1984.
[86] G. Ben-Dor, O. Igra, and T. Elperin, *Handbook of Shock Waves*. New York: Academic Press, 2000.
[87] R. S. Tranter and P. T. Lynch, “A miniature high repetition rate shock tube.,” *Rev. Sci. Instrum.*, vol. 84, no. 9, p. 094102, Sep. 2013.
[88] Philip Laven, “MiePlot.” 2015.
[89] A. J. White and M. . Hounslow, “Modelling droplet size distributions in polydispersed wet- steam flows,” *Int. J. Heat Mass Transf.*, vol. 43, pp. 1873–1884, 2000.
[90] J. Porstendörfer, H. G. Scheibel, F. G. Pohl, O. Preining, G. Reischl, and P. E. Wagner, “Heterogeneous Nucleation of Water Vapor on Monodispersed Ag and NaCl Particles with Diameters between 6 and 8 nm,” *Aerosol Sci. Technol.*, vol. 4, no. November 2015, pp. 65–79, 1985.

Appendix Engine Standard Operation Procedure

Engine Mounting

1. Place the aluminum holder onto the aluminum bread board; fix it by four metal 90° angle brackets.

2. Use 4 × #6 socket screws to fix the engine onto the holder.

Standard Operation Procedure

Mixing Fuel

1. Put on rubber gloves.

2. Take out methanol and castor oil from the Flammable Liquid Storage Cabinet.

3. Pour 900ml methanol and 100ml castor oil into a 1000ml capacity beaker. Then put the bottles back.

4. Mix the fluid using a magnetic blender.

5. Using a funnel to pour the mixture into the fuel tank.

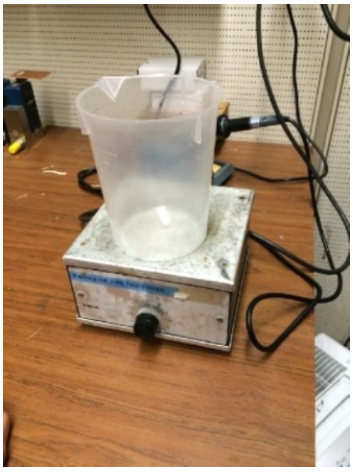

Magnetic Blende

Before Starting the Engine

1. Check if the starter' and glow-plug's battery are still working; if not, fully charge them before starting the engine.

2. Check if there's enough fuel in the fuel tank (for reference, the fuel consumption rate at 3500 r.p.m. is 6oz/h). If not, fill enough fuels.

3. Check the tightness of the screw on the engine head; if loose, tight it before starting.

4. Fasten the stripes on the fuel tank holder, close the needle valve on the calibrator, remove two flow stoppers, and connect the upper tube to the port on the muffler and the lower one to the calibrator.

5. Start the thermostat and run the cooling circulation at 10℃.

6. Turn the lab's vacuum blower to the high level.

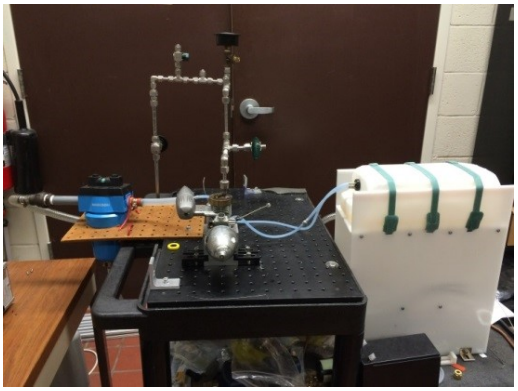

Experiment Table Overview

Thermostat Back Panel

Vacuum ump

Starting Engine

1. Before starting the engine, rotate the engine head with hand. If the resisting momentum is too large, take off the cylinder head and check if there's too much liquid in the cylinder.

2. Fix the cord for the air throttle lever to a position that the lever is 20° left off vertical when viewed from the left side. Connect the starter to its battery. Connect the glow plug to the cylinder head. Turn the needle valve on the calibrator anti-clockwise to open by rotating about 3 times.

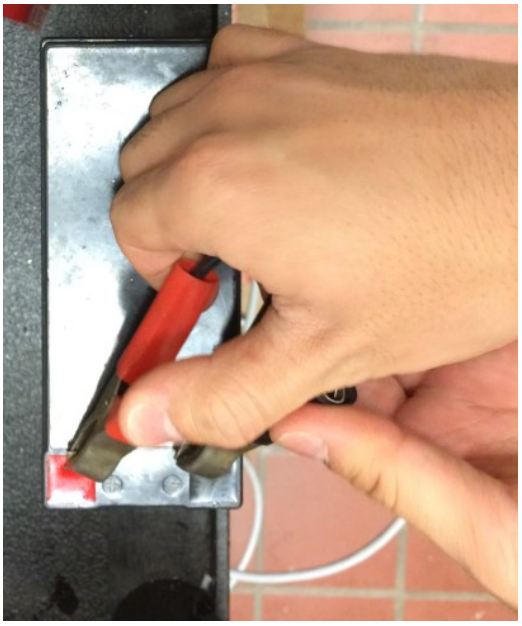
Connecting the Starter to Battery

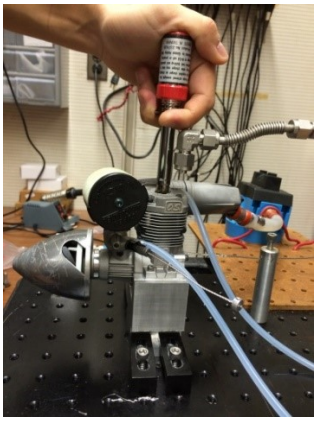

Connect the Glow Plug to the cylinder head

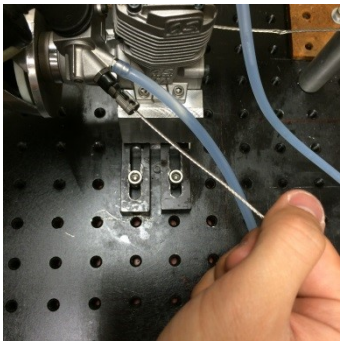

Turning the Needle Valve Anticlockwise

3. Run the starter without load for 2s then press the rubber cup against the engine head.

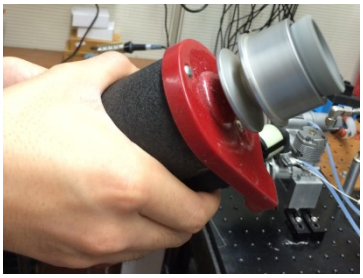

Running the starter without load

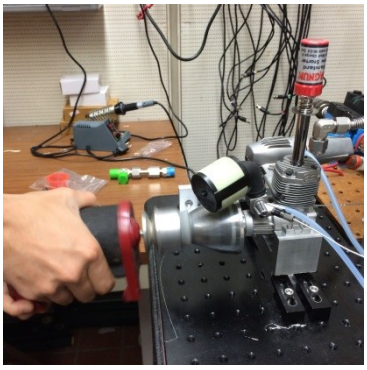

Pressing the Rubber Cup against the Engine Head

4. Normally, the engine will start. If the engine doesn't start after applying the starter for 5s, remove the starter and fasten the engine head screw then make a second attempt. If too many attempts fail, remove the crankcase cover to release the accumulated fuel in the crankcase. Also wipe the cylinder head's lower surface, as too much liquid covering the glow plug will stop the glow plug from ignition.

5. If the engine hasn't been used in the past 20 min, keep the glow plug connected to the cylinder head for 10 seconds after the engine starts.

6. Close the air throttle gradually. A drop in the noise pitch will be observed. The normal sound of the engine should be a muffled exhaust noise. If you hear a succession of explosive sound, stop the engine (you should stop the engine in the right way mentioned in the next section.) and take off the cylinder head and crankcase cover to check if there's too much liquid in the cylinder.

7. Use the tachometer and adjust the throttle to keep the engine running at 3500 ± 150 r.p.m. If the engine doesn't run stable enough, open the calibrator needle valve a bit.

After Experiment

1. When the experiment is finished, stop the engine by closing its air inlet. Never stop the engine by closing the needle valve.

2. After the engine stops, close the needle valve instantly.

3. Remove the fuel lines from the engine and put stoppers into the tubes. Put the fuel tank back into the Flammable Liquid Storage Cabinet;

4. Keep the cooling water running for an extra 5 minutes to condense all methanol in the exhaust line. Dispose methanol into the glass container container labeled with GENERAL WASTE (NO HELOGENS), record the disposals on the HAZARDOUS WASTE sheet, and dispose condensed oil into the plastic bucket.

5. Turn off the thermostat and clean the experiment table.

Monthly Maintenance

Monthly maintenance is required to remove condensed oils and particles.

1. Disassembly the engine. The right disassembly sequence is: muffler, crankcase cover, cylinder head, cylinder sleeve (do not scratch its inner surface), piston, calibrator, engine head screw, engine head threaded spacer, pull the shaft out from rear.

2. Put these parts into the ultrasonic cleaner and close the outlet valve; Add water and soap to immerse all parts; Set the temperature at 30℃ and turn on the cleaner for 1 hour; if some of the parts are still greasy, wash them for an extra 30 minutes.

3. Dry all parts instantly; Take care when drying the two bearings as they are easy to rust; never soak parts overnight.

4. Before assembling these parts together, add castor oil to the bearings and cylinder sleeve; 1~2 drops for each place.

5. Assemble the parts in the reverse order in Step 1; when pushing the sleeve into the engine body, make sure the small groove on the sleeve coincide with the reference pimple on the engine body.

6. Rotate the engine head with hand; feel with your hand if there’re points where the resistance is too big; listen carefully if there’re abnormal noises. If the engine doesn’t rotate smoothly, take off the crankcase cover and the calibrator and see if there’s still residual water.

7. After the engine could rotate smoothly with hand, start it in the way mentioned in Section Ⅱ.

Let the engine run in for 15mins.

Disassembling the Engine

Ultrasonic Cleaner